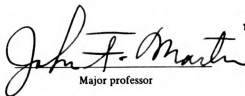This is to certify that the

thesis entitled

INVESTIGATION OF SURFACE STRAINS IN
FIR TREE TURBINE BLADE ATTACHMENTS

presented by

Captain Joseph P. Marksteiner

has been accepted towards fulfillment
of the requirements for

M. S. _____ degree in ___ MMM ___

John F. Martin
Major professor

Date 11/15/85

O-7639

INVESTIGATION OF SURFACE STRAINS IN
FIR TREE TURBINE BLADE ATTACHMENTS

By

Captain Joseph P. Marksteiner

A THESIS

Submitted to
Michigan State University
in partial fulfillment of the requirements
for the degree of

MASTER OF SCIENCE

Department of Metallurgy, Mechanics and Materials Science

1985

ABSTRACT

INVESTIGATION OF SURFACE STRAINS
IN FIR TREE TURBINE BLADE ATTACHMENTS

By

Joseph P. Marksteiner

Surface strains in the fillet regions of test model specimens of fir tree turbine blade attachments were examined. The fir tree specimens are loaded under cyclic tension-tension in the elastic range. The strains were recorded with an interferometric technique at the center and near the edges of the exposed unloaded face of the fir tree. Data were recorded for a total of over 700 load cycles on 23 different specimens. Two different load bearing surface geometries were investigated. The effect of machining tolerances were determined for both geometries. The load split between the two sets of load bearing surfaces was determined. Actual strains were compared to those predicted by superposition of strain fields. Stresses computed from the recorded strains were compared to photoelastic and finite element analyses.

ACKNOWLEDGMENTS

TABLE OF CONTENTS

TABLE OF CONTENTS (Continued)

LIST OF FIGURES (Continued)

LIST OF FIGURES (Continued)

CHAPTER I

INTRODUCTION

In recent years there has been an increased demand placed upon aircraft powerplant manufacturers to provide more efficient engines. A major part of this effort has been dedicated to investigating the limitations of the materials and structures used, especially in the "hot section" of the engine (1)*. Hot section components include the combusters, turbine blades, vanes, and disks. All operate under extremely high temperatures and severe loads even at low engine power.

Improvements in design result from testing existing components and with those data, developing new and better materials and structures to cope with the adverse operating conditions involved. Prior to implementing any new design, extensive testing is required to determine whether it is better than its predecessor and if so, how much.

Design criteria for turbine blades are based on the expected operating temperature and cyclic loading conditions. Figure 1 shows a typical stress-range diagram for a turbine blade material. The turbine blade itself

---

*Numbers in parentheses refer to references listed in the reference table. Numbers in brackets refer to equations.
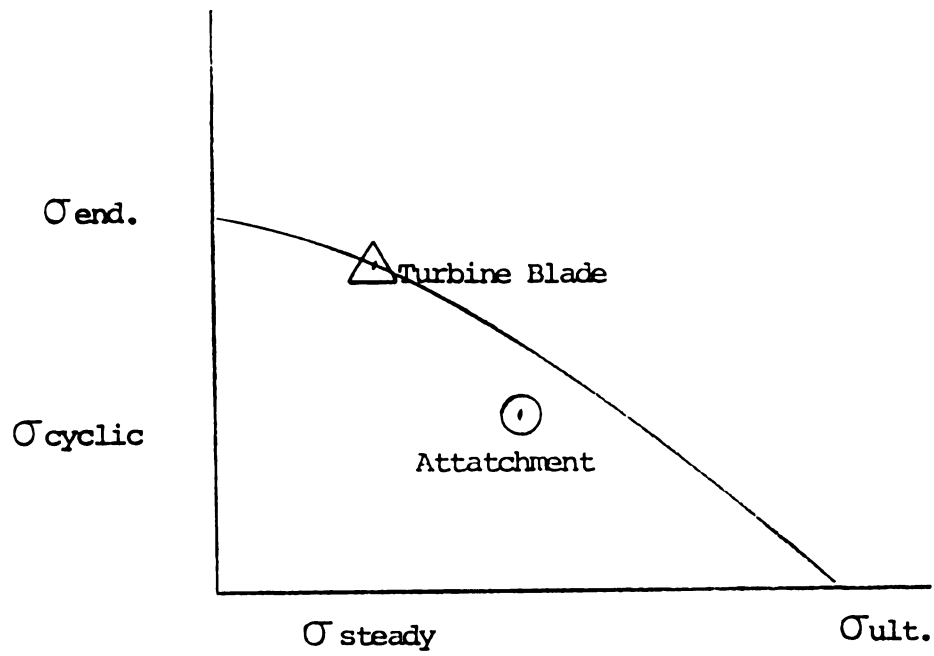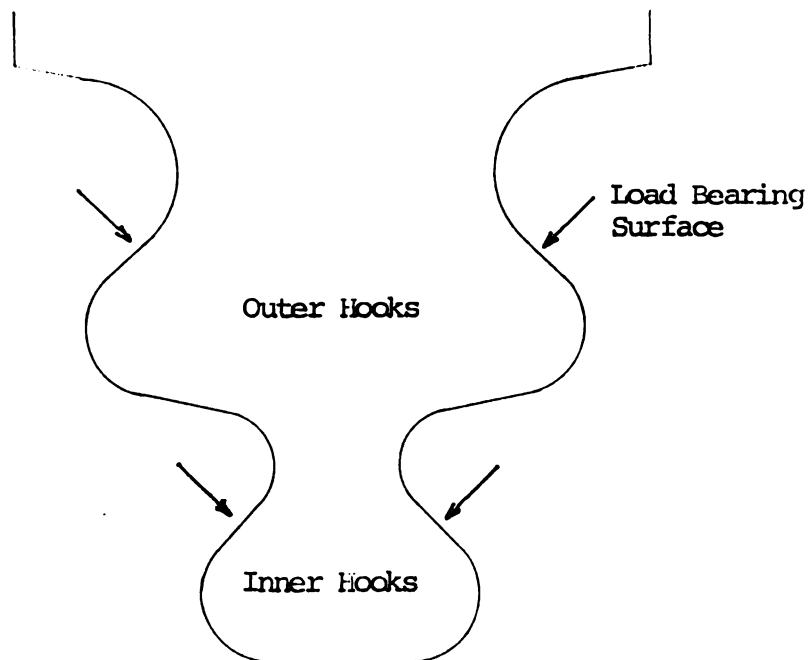
Figure 1   Stress Range Curve

Figure 2   Fir Tree Attatchment

operates on the limit of the curve, so that it will theore-
tically fail near its design life. The attachment however,
is usually designed so that it falls somewhere within the
limits of the curve (2). Recently, however, advancements in
turbine design and coating technology have made the blade
attachment region the life limiting factor (3).

A modified two tang fir tree turbine blade attachment
of directionally solidified MAR 247, which a nickel based
super alloy, is in the initial stages of testing and is
being compared to the current design of the same material.
The basic design of the fir tree attachment is shown in
Figure 2. It consists of two sets of tangs or "hooks". The
designation of inner or outer refers to the position the set
occupies in relation to the center of the turbine disk. The
indicated load bearing surfaces are planes in both the fir
tree and turbine disk for the current design geometry.
Theoretical data compiled by Garrett Turbine Engine
Company** using finite element methods (4) based on contact
stress studies conducted by J. O. Smith and C. K. Liu (5),
indicate a possible 10 fold increase in fatigue life for a
crowned geometry of the fir tree load bearing surfaces.

Both the initial finite element model used by Garrett
and predictions based on photoelastic theory are two
dimensional in nature. The fir tree attachment however,
approximates a right cylinder with the loads applied on the
lateral boundary, and no assumed deformation along the axis

**A division of Garrett Corporation, Phoenix, Arizona.

of the cylinder. This, according to Sokolinikoff (6) falls into the class of plane strain problems. The two dimensional approach is justified by Durelli and Wiley (7) by assuming that separate slices of the blade attachment are essentially two dimensional and that the load carried by each slice is different. Data collected in photoelastic studies on thin sheets compared very well with actual test results and validated this assumption.

The actual stress state in the fir tree attachment is extremely complex. The complexity is due not only to the geometry of the attachment but to the loads appled to it. Stresses are due to the bending and twisting moments that result from the aerodynamic forces on the blade and are superimposed on the stresses caused by centrifugal tension in the fir tree.

The purpose of this study is to directly determine the actual surface strains on the face of the fir tree specimens under tensile load conditions. This will simulate the centrifugal forces on the blade attachments in the engine. Strain measurements will be made with an interferometric strain measuring technique. These data will be used for three purposes. The first will be to characterize the effects of machining tolerances on load distribution. Second, the load split between the two sets of load bearing surfaces will be determined. Third, it will be determined whether the principle of superposition of strain fields accurately predicts surface strains. Finally, surface

stresses calculated from the strain data will be compared to photoelastic studies and finite element model analyses.

CHAPTER 2

INTERFEROMETRIC STRAIN GAGE

2.1 Fundamentals of the ISG

An Interferometric Strain Gage (ISG), which is a noncontact laser device, was used to measure surface strains (8-11). The ISG is able to measure strains over very small gage lengths, typically 100 microns. The device measures strains by monitoring the position of interference fringe patterns generated by pyramidal indentations in the surface of the specimen. These indentations are made with a Vicker's Micro Hardness Tester and measure approximately 25 microns across. Figure 3 shows a schematic diagram of the indents and the incedent laser light. Interferring rays of light are out of phase by $d \sin \alpha$ where α is the angle between the incedent laser beam and the reflected interferring rays. Whenever the following relationship is satisfied:

$$d \sin \alpha = n\lambda \quad (n = 0,1,2,...) \tag{1}$$

where λ = wavelength of the laser light

The reflected rays are constructively in phase and a bright spot in the fringe pattern will be caused. Figure 4 shows a typical fringe pattern. Due to symmetry, two identical fringe patterns will be created, Figure 5. When observed from any stationary point, defined by α_{og} any movement of
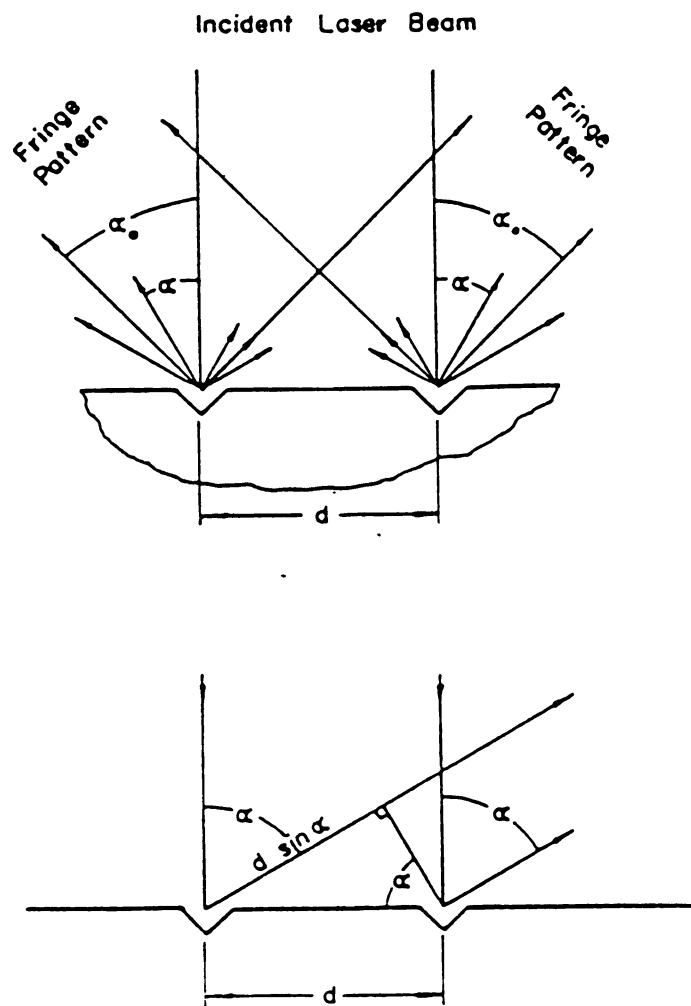
Incident Laser Beam

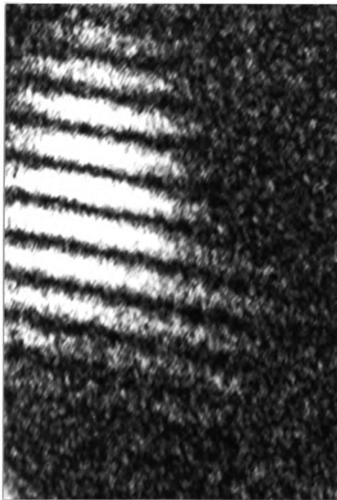Figure 3   Indent and Laser Schematic   (8)
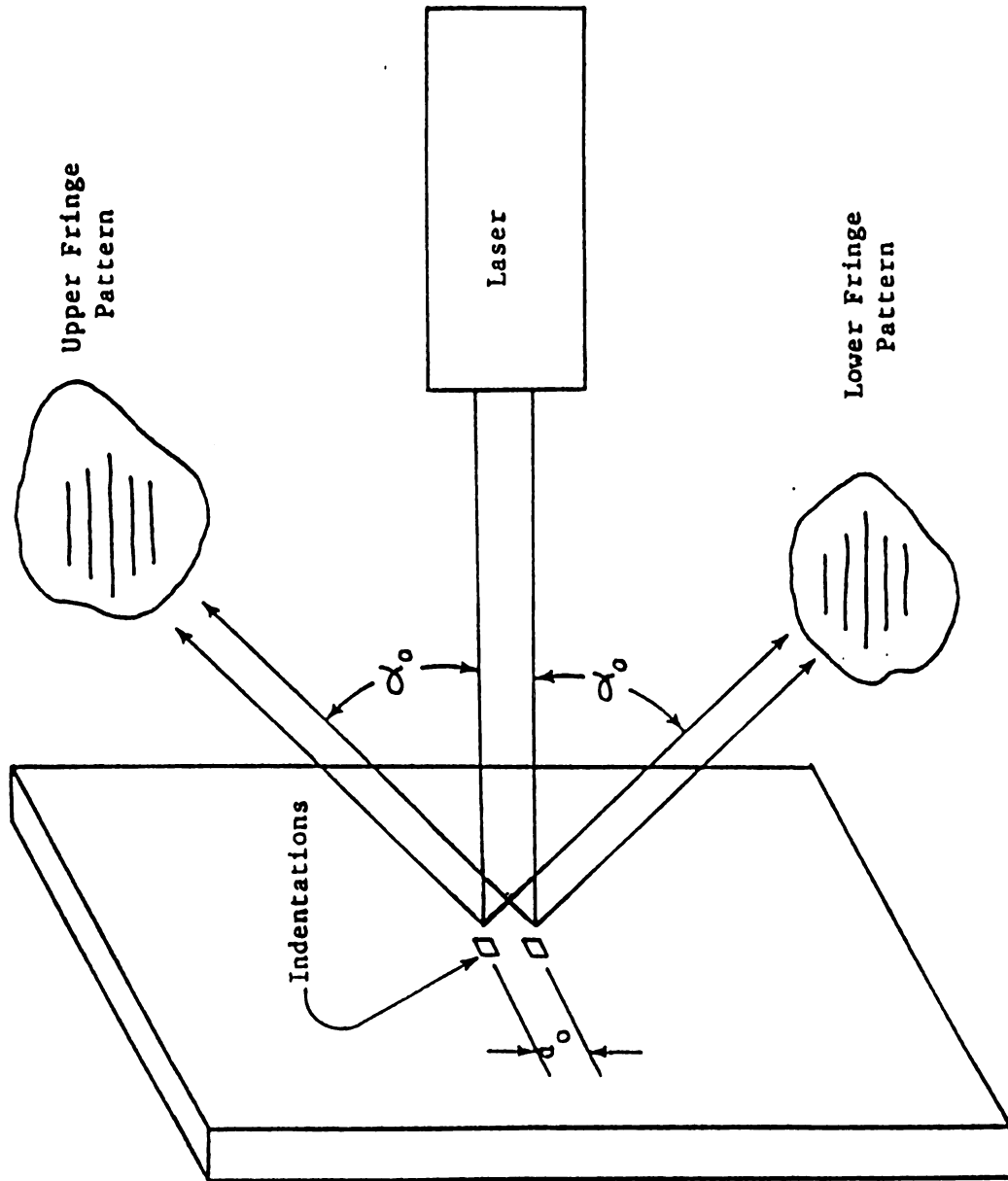
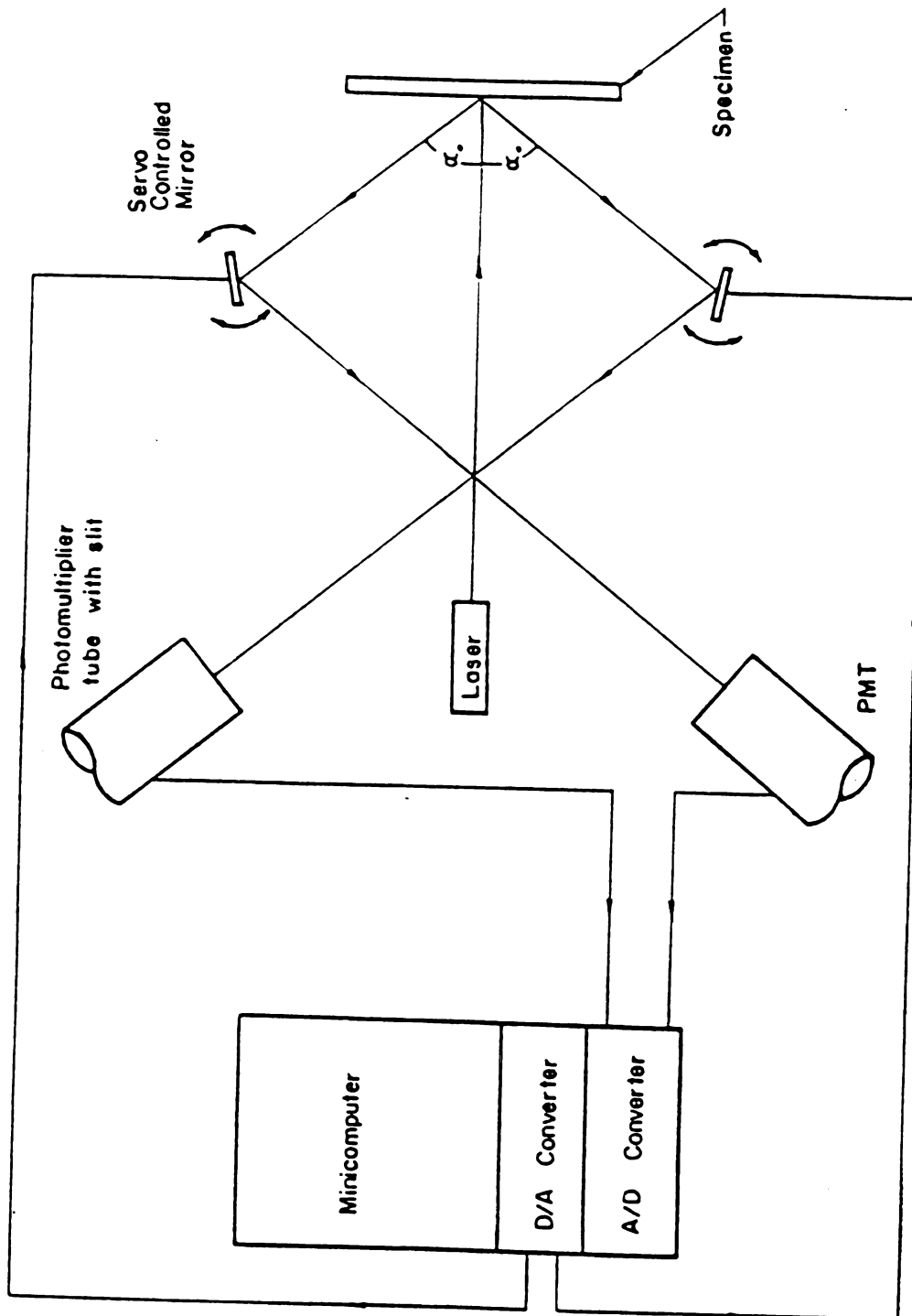Figure 4 Interference Fringe Patterns

Figure 5   Fringe Pattern Orientation

Figure 6   ISG Schematic

the indentations is seen as a fringe shift. For any single fringe in the pattern, dsin α is a constant determined by the order n, in equation [1]. An increase in d (tensile strain) will cause the fringe patterns to shift toward the incedent laser beam, while a decrease in d (compressive strain) will shift the fringe patterns away from it. For rigid body motion along the same axis as the indentations and fringe patterns, one set of fringes will move toward the laser beam while one set will move away. If these motions are assigned positive and negative signs respectively, then averaging them will cancel rigid body motion.

The relationship between fringe movement and strain causing indentation motion is:

$$\Delta d = \frac{\lambda}{\sin \alpha_O} \Delta m \qquad [2]$$

Where 'm' is the number of fraction of fringes passing the fixed observation point defined by α_O. The average motion of the two generated fringe patterns is:

$$\Delta d = \frac{\lambda}{\sin \alpha_O} \left(\frac{\Delta m_1 + \Delta m_2}{2} \right) \qquad [3]$$

2.2 ISG Hardware and Software

A schematic diagram of the ISG is shown in Figure 6. Two servocontrolled mirrors are positioned in the interference fringe patterns defining the angle α_O. These mirrors sweep a portion of the fringe pattern across the face of the photomultiplier tubes (PMT's). Each tube is
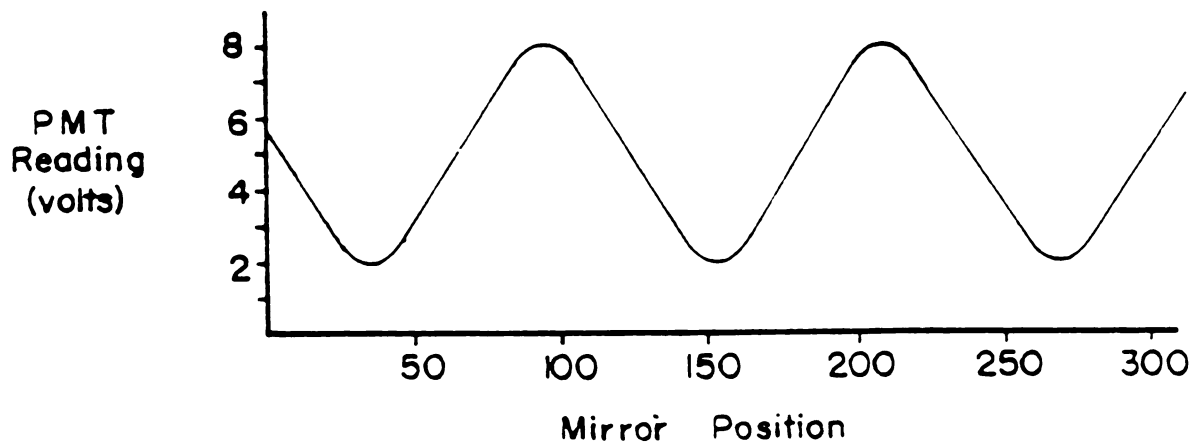
Figure 7   PMT Voltage vs. Mirror Position

masked by a cover with a narrow slip parallel to the bars of light in the fringe patterns, so that only one bright fringe can shine through at a time. The sweep of the mirrors is governed by a ramp generator and a plot of time versus voltage output from the "PMT's has a sine wave appearance, with higher voltage corresponding bright spot in the fringe. A minicomputer divides this data into 256 locations and stores the PMT output voltage for each one, as shown in Figure 7. During loading of a test specimen, the shift of fringes is updated every 100 milliseconds. Any change in fringe position is converted to an analog voltage by the computer that is directly proportional to strain at the indentations. This output voltage is determined by the strain and preset parameters in the controlling program and obeys the following equation:

$$mv = (\varepsilon \ s \ d \ \sin \ \alpha \ (9.76) \ gain)/\lambda \qquad [4]$$

where ε = strain, s = average spacing between peaks in Figure 7, d = distance between indents, gain is a computer parameter between 2 and 8.

For a given strain the output voltage can easily be computed. This voltage is then run through an analog computer and is used to calibrate recording equipment. The ISG output is fed through the analog circuit and to the recorder and can be read directly as strain.
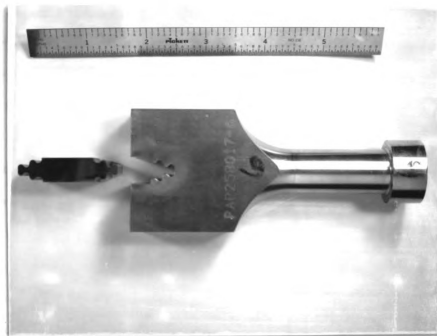
14

Figure 8   Test Specimen & Loading Fixture

CHAPTER 3

LOAD TRAIN

3.1 Load Fixtures and Load Train

Test specimens and loading fixtures supplied by Garrett
are shown in Figure 8. The design of the loading fixtures
and the specifications of the test program required a
multicomponent load train. The load fixtures were mounted
in modified compression grips, designed to accommodate the
button heads on the test fixtures. Universal joints were
used to attach the compression grips to the hydraulic ram
and the load cell. The universal joints were needed to
allow for orientation changes between the fir tree and the
loading fixture. Orientation changes would result from
shifting and slipping of the contact surfaces predicted by
Heywood (12). The complete load train is depicted in Figure
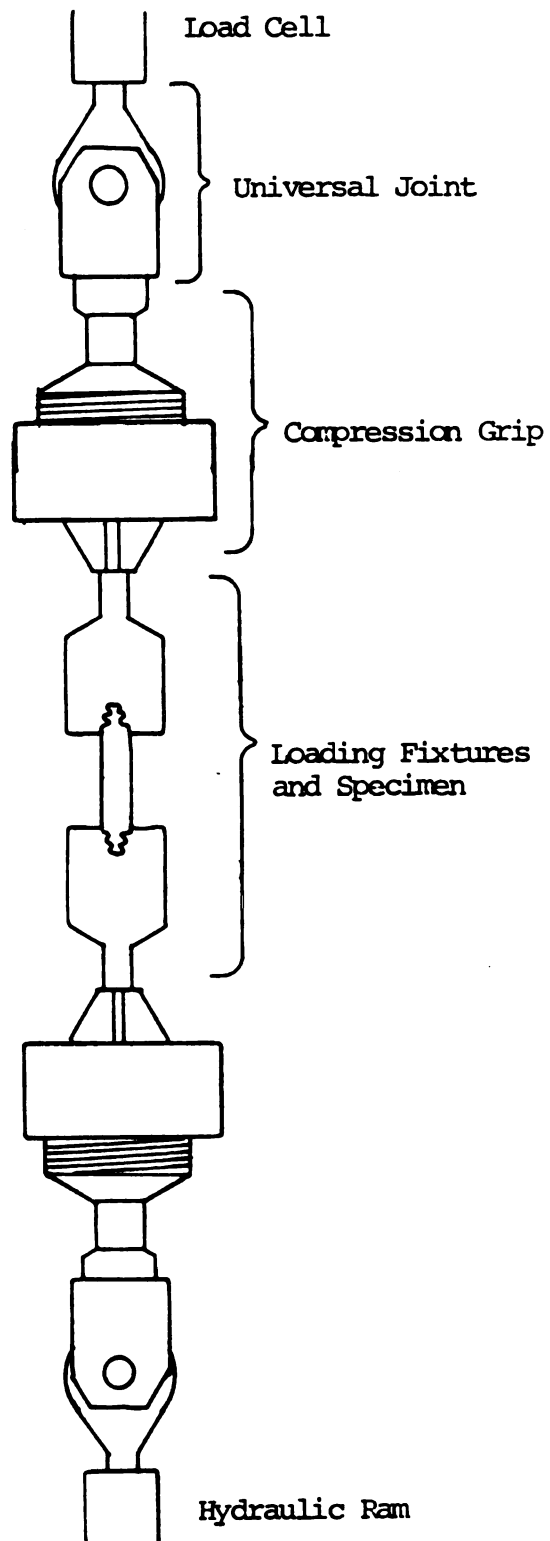9.

Load Cell

Universal Joint

Compression Grip

Loading Fixtures
and Specimen

Hydraulic Ram

Figure 9   Complete Load Train

CHAPTER 4

SPECIMEN PREPARATION

4.1 Surface Preparation

The specimens supplied by Garrett were prepared in the same manner as the actual turbine blade attachments. The shape of the fir tree was produced by very accurately shaped grinding wheels. To inhibit crack initiation the entire surface was shot peened. This greatly reduced the reflectivity of the specimen and consequently would have added to the difficulty of producing data with the ISG.

The shot peened face of the crowned specimens was polished with progressively finer abrasives until it was highly reflective. The specimens with the flat load bearing geometry were supplied with a very large bevel on the edges. On several of the specimens, the bevel extended approximately 25% across the small fillet region, Figure 10. The faces of the flat specimens were ground down until the remaining bevel was the same as the crowned specimens. This grinding reduced the cross-sectional area of the flat specimens approximately 1%. In all direct comparisons between the crowned and flat geometries, this area reduction was accounted for.
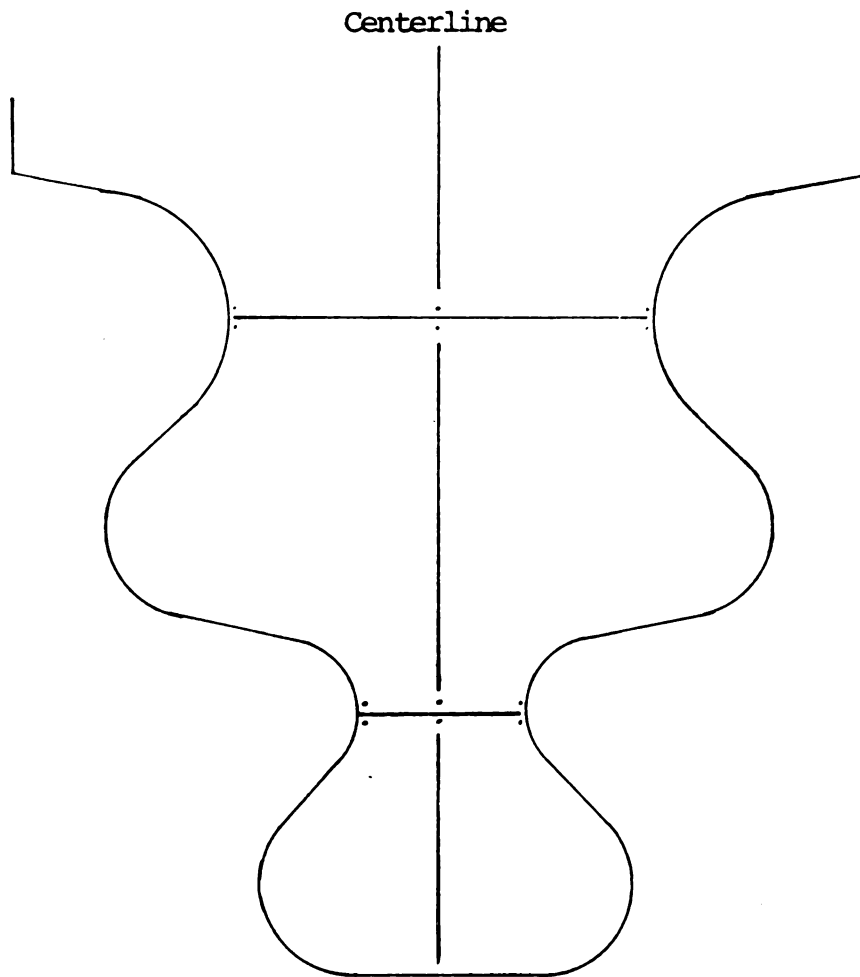
Figure 10   Flat Specimen Edge Bevel

Figure 11   Indent Locations

4.2 Indentation Placement

Indentations for the interferometric strain measurements were made on the polished faces of the specimens with a Vicker's Microhardness Tester. Three sets of indentations were placed along a horizontal line joining the innermost edges of each fillet region, Figure 11. They were placed in the center of each fillet and 50 microns from the inside edge of the bevel.

The indentation locations were chosen in the fillet region for several reasons. First, the material was directionally solidified along the radial or Y axis of the fir tree. Young's modulus data was available only for this axis. Second, the principal stresses in the fillet region were nearly identical to the radial or Y-direction stresses in two separate finite element analyses conducted by Garrett (3 and 4). Additionally, the Y axis of the specimen, the tensile axis and the strain measurement axis of the ISG were all aligned in the same direction. Finally, the micro hardness tester used to make the indentations was not equiped with a rotating table. Placement of indentations along any axis other than vertical or horizontal would have been innacurate and inconsistent.
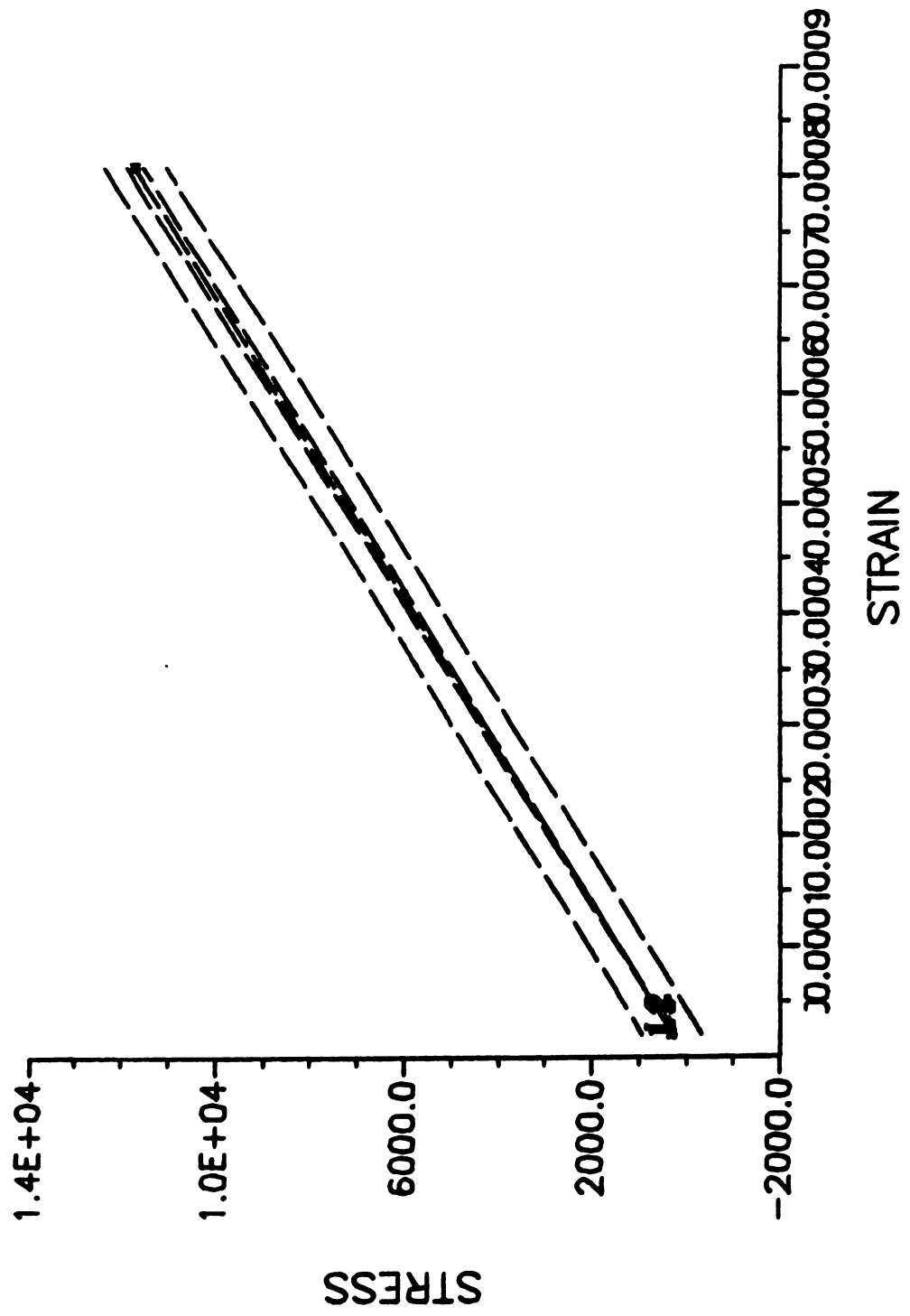
Figure 12 Tensile Modulus of Specimen

CHAPTER 5

TEST PROCEDURES

5.1 Determining Young's Modulus

To test the alignment of the load train and the
accuracy of the ISG, the tensile modulus of the specimen in
the longitudinal direction was obtained. Indentations were
placed in the center portion of a test specimen equidistant
from each of the fir tree ends. ISG strain versus load data
were produced. The center of the specimen was assumed to be
analogous to a smooth bar with a rectangular cross sectional
area (0.32 square inches). From the strain versus load data
Figure (12), and the previous assumption, a modulus of 15.8
x 10^6 for the tensile direction of the specimen was
computed. The Young's modulus was reported at 15.92 x 10^6
(13).

All test specimens were initially tested at relatively
low loads (4500 lbs) compared to the actual fatigue loads
(11,750 lbs) that were used in later stages of the test
program. The low loads were chosen to prevent any plastic
deformation and to ensure that rigid body motion of the
specimen did not move the indents out of the area
illuminated by the laser. Rigid body motion effects are
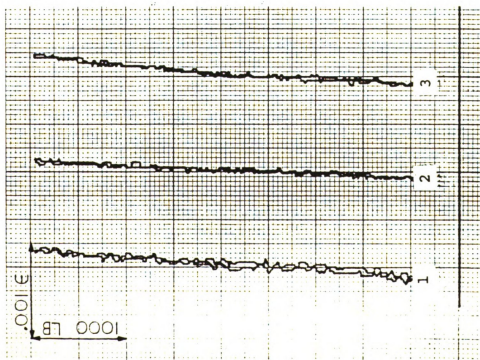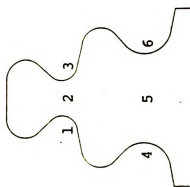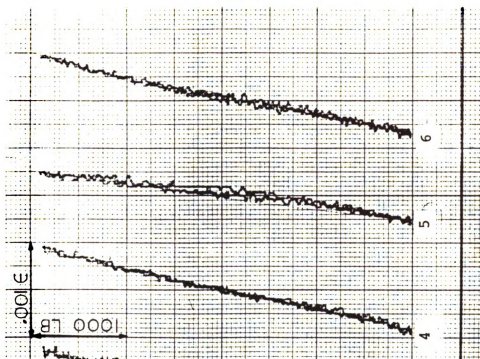discussed in detail in Appendix 1 of this report.

22

Figure 13   Data Locations

5.2 Characterization of Effects Due to Machining

    Tolerances

Photoelastic studies indicate that stress imbalances as
high as 50,000 psi may result from the misfit produced by
allowable machining tolerances between the fir tree and the
disk (7).

Load versus strain data were produced for six locations
on the unloaded face of the fir tree on each end of the
specimen as shown in Figure 13. Because of the symmetry of
the ends of the specimens, this produced two data sets per
specimen.

These characterization data revealed some trends that
were completely unforeseen. On some specimens the load
versus strain data is very linear at all locations. It
qualitatively reflects stress and strain distributions that
would be expected across the fillet region as shown in
Figure 14. These data also fit the predicted stress
distribution produced by the finite element studies and
photoelastic distributions for similar shapes.

Even though the specimens were loaded in cyclic
tension-tension, a large number of the strain plots showed
compression. The data, initially seemed illogical. The
first specimen to show this tendency was removed from the
loading fixtures, reindented, and then retested. But the
same data resulted. The opposite face of the specimen was
indented and tested, and the results agreed with the
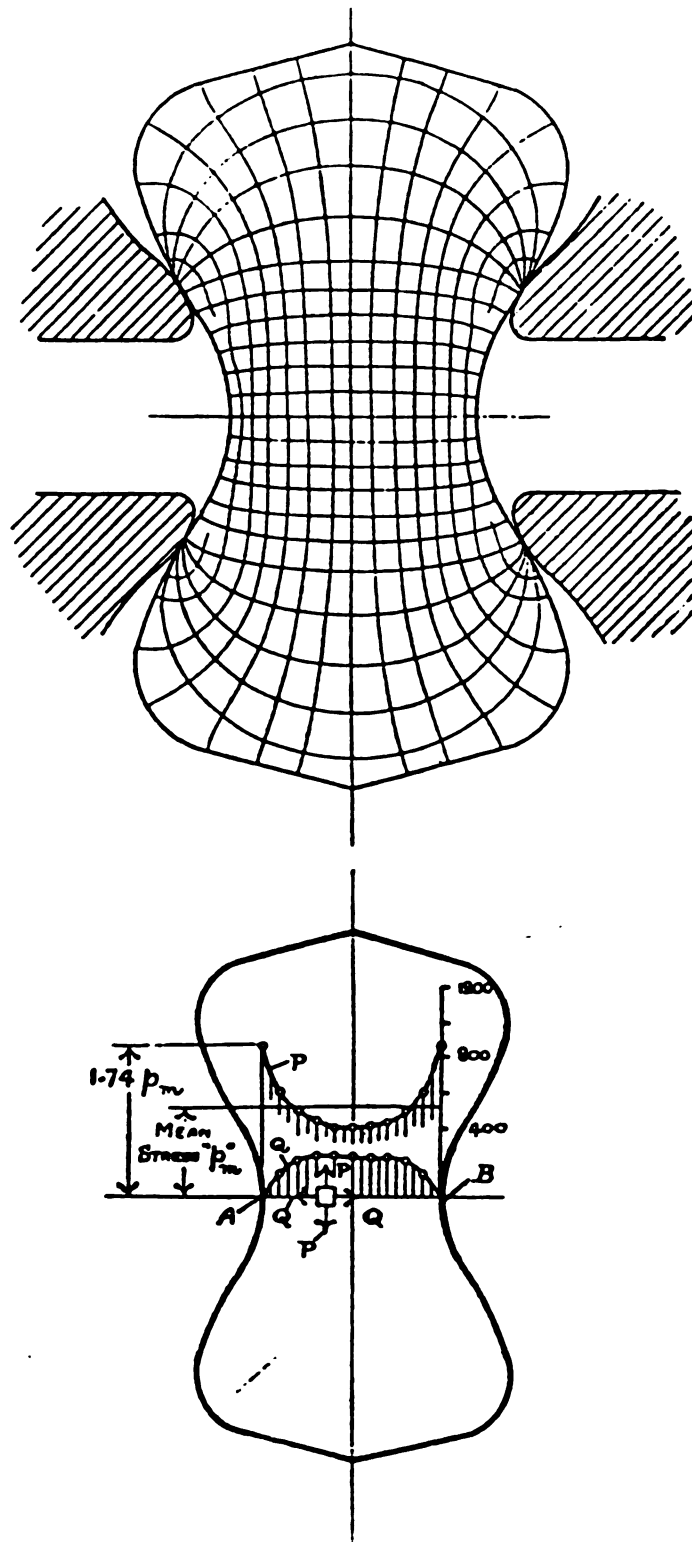previous data. The data from the three sets of indents

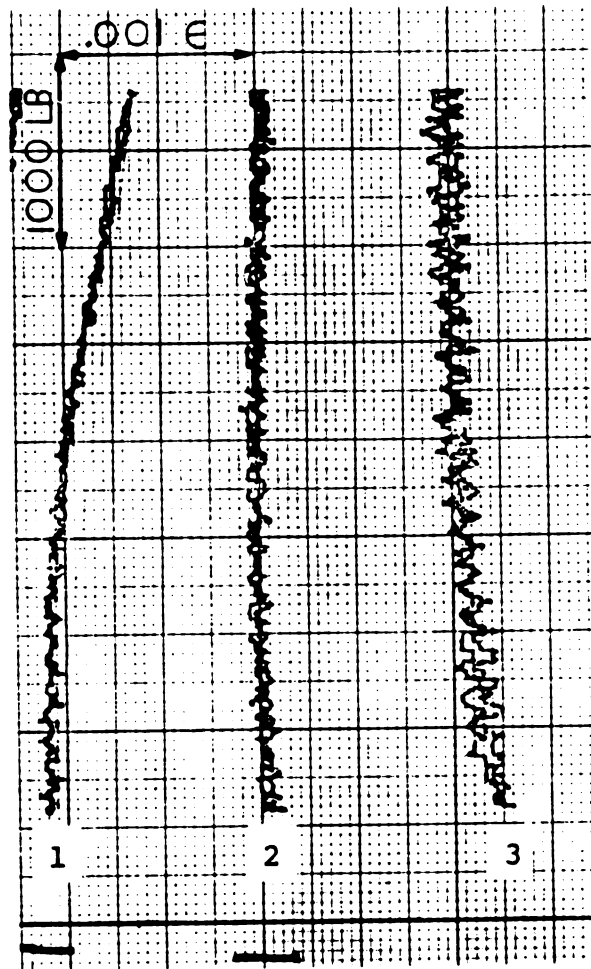Figure 14   Photoelastic Stress Distribution (13)

Figure 15   Compressive Strain in Fillet

Tensile   Bending   Resultant
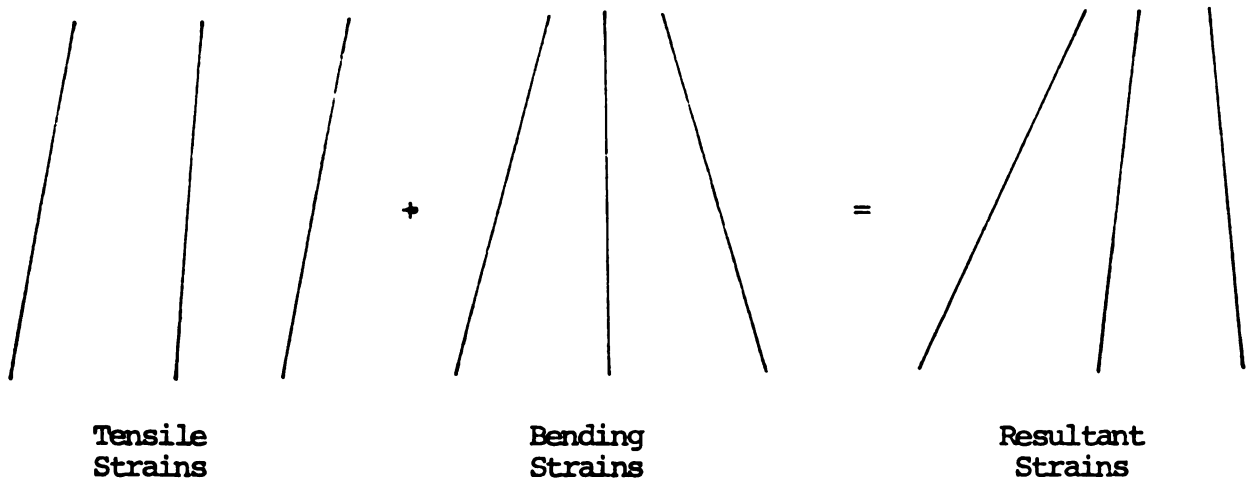Strains   Strains   Strains

Figure 16   Superposition of Strains

across the inner fillet in Figure 15 illustrate this phenomenon. It was assumed that the combined effects of machining tolerances at the four load bearing surfaces could cause a bending stress field across the fillet region. Figure 16 demonstrates how a pure bending stress distribution superimposed on a tensile stress distribution would produce the observed load versus strain data. With the much smaller cross sectional area and moment of inertia at the inner fillet, any bending stresses that were produced by machining effects would show prominently in this area. If the bending moment caused by machining tolerances is assumed to be equal in each of the fillet regions, then a simple calculation of the relative stresses can be made. The following calculation compares the maximum stresses due to bending at the inner and outer fillet regions.

$$\sigma = \frac{My}{I}, \quad \sigma_I = \frac{M(.0914/2)}{\frac{1}{12}(.8)(.0914)^3} = 898 \ M,$$

$$\sigma_o = \frac{M(.234/2)}{\frac{1}{12}(.8)(.234)^3} = 137M$$

[5]

Bending stresses in the inner fillet were clearly exhibited in 10 of 16 crowned specimens and 4 of 7 flat specimens.

Some of the data exhibited a cyclic pattern as shown in Figure 17. The figure shows the load versus strain plots for the right edge, center, and left edge of the inner fillet, respectively. The arrows shown how the load was
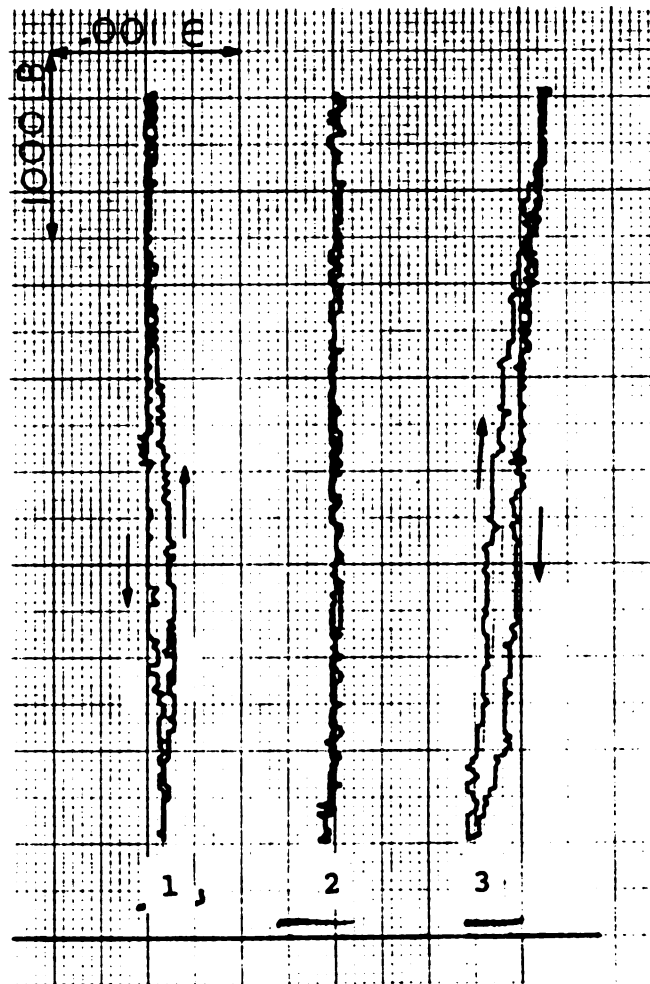
Figure 17   Cyclic Strains

changing during that portion of the plot. The center plot indicates that the stress at that point is linearly changing with load. The two edge plots indicate two values of strain for the same load, depending on whether the load was increasing or decreasing. The general shape would suggest a hysteresis loop, but the loading is strictly tensile. The cyclic shape can be explained by slipping of the contact surfaces as predicted by Durelli & Wiley (7). On the linear side of each loop, the point of load application is not changing. The nonlinear side indicates that there is slipping of the contact surfaces during the loading cycle. It was also noted that when there was slipping of the contact surfaces, one surface remained fixed while the other shifted. For the crowned geometry specimens, slipping will not affect the point of load application in the fir tree. An analysis of the fixture similar to that carried out for the fir tree shows that a change of load position on the fixture will change the magnitude of the load applied to the fir tree.

Additionally, the surface strains for the given loads indicated that in all the specimens only a very small percentage of the total load was carried by the material near the surface of the unloaded face. The problem was further complicated by the fact that the specimens had a fir tree at each end. Reactions at one end of the specimen that caused some change in alignment between the fir tree and the
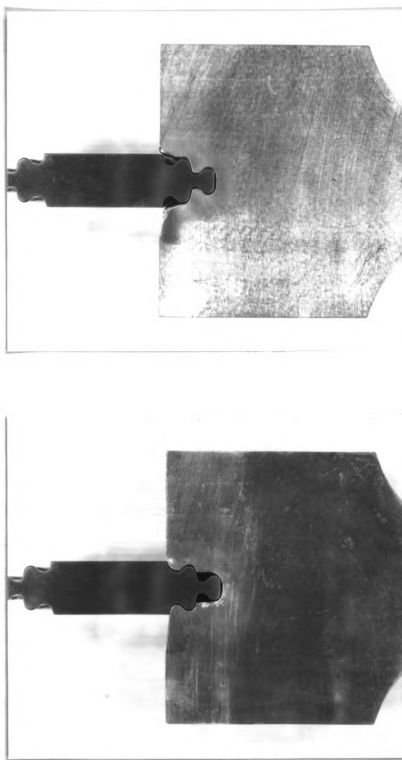
Figure 18 Partial Fixtures

fixture, could not be separated from the reactions at the other end.

5.3 Load Split Determination

To simplify the problem of determining the load split between the inner and outer set of hooks, a set of loading fixtures were cut as shown in Figure 18. One fixture would only apply load to the inner set of hooks, while the other fixture would only apply load to the outer set. Three specimens from each geometry were run in the partial fixtures. Both ends of the specimens were tested in each cut fixture. This generated two data sets for each end of a specimen.

When the inner hooks were loaded, the exact strains across the neck for a given load (4500 lbs) were determined. The inner hook strains resulted from the neck stress and the superimposed hook stress field. The strains across the outer fillet were also recorded. These strains were the result of tensile neck stresses, without the superimposed hook stress field. Typical plots for strains in the neck regions are shown in Figures 19 and 20. When the outer hooks were loaded, the recorded strain versus load plots reflect both neck and hook stress fields.

The mean stress in the outer fillet was the same whether the inner or outer hooks were loaded. The stress distribution as expected for each of these cases was different. The most noticeable difference was in the center of the fillet. When loaded at the outer hooks, the
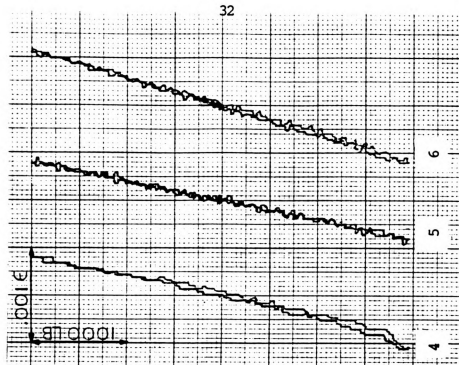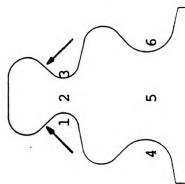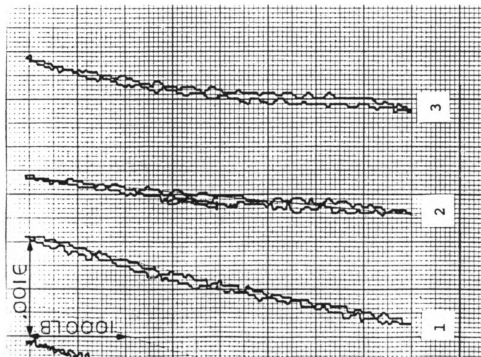
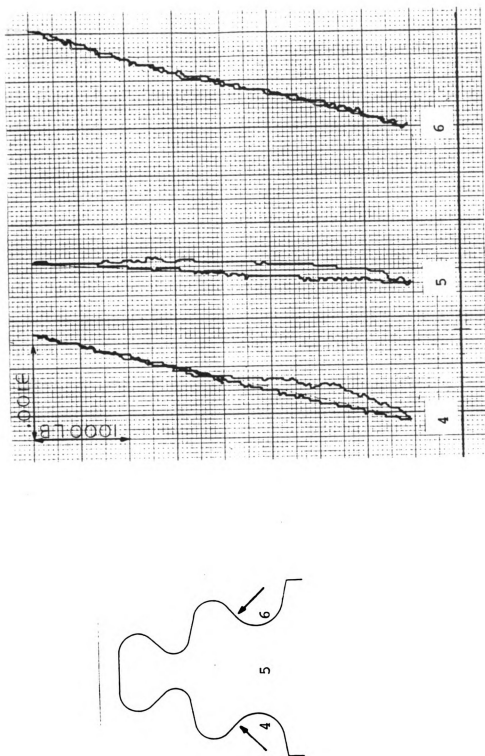Figure 19   Inner Hook Load Partial Fixture Strains

Figure 20   Outer Hook Load Partial Fixture Strains

average strain in the center is nearly zero. For the mean

stress across the cross section to be the same, an increase

in the stress concentration at the edge of the fillet is

required. This indicates that hook loading has a greater

contribution to stress concentrations in the fillet than

neck loading.

It was assumed that if a given load on the inner hooks

produced a certain strain in the partial fixture data, then

that same strain would indicate the same load on the inner

hooks during the high load tests. Data were compared for

the three indent locations across the fillet and averaged to

compute the load carried by the inner hooks. By simple

subtraction the remaining load carried by the outer hooks

was computed. Figure 21 shows this process and Figures

22-27 graph the actual data.

5.4 Superposition of Strain Fields

The principle of superposition is widely used to

simplify problems with combined stress fields (6). The

strains measured at the edge of the outer fillet were used

for the superposition testing. These strains were large in

magnitude than the center strains which improved the

accuracy of the measurements. To eliminate errors caused by

bending stresses, the average value of these strains was

used in the computations. To determine if the principle

held, the process depicted in Figure 28 was followed.

First, with the load split previously determined, the outer
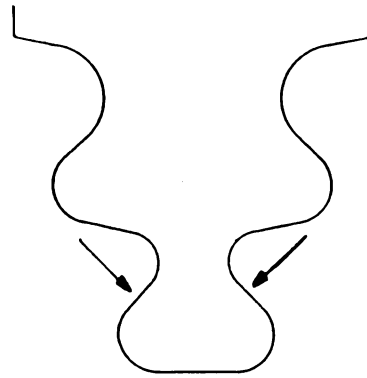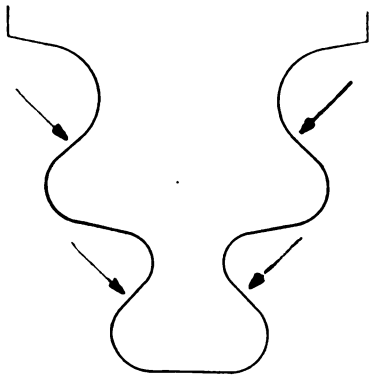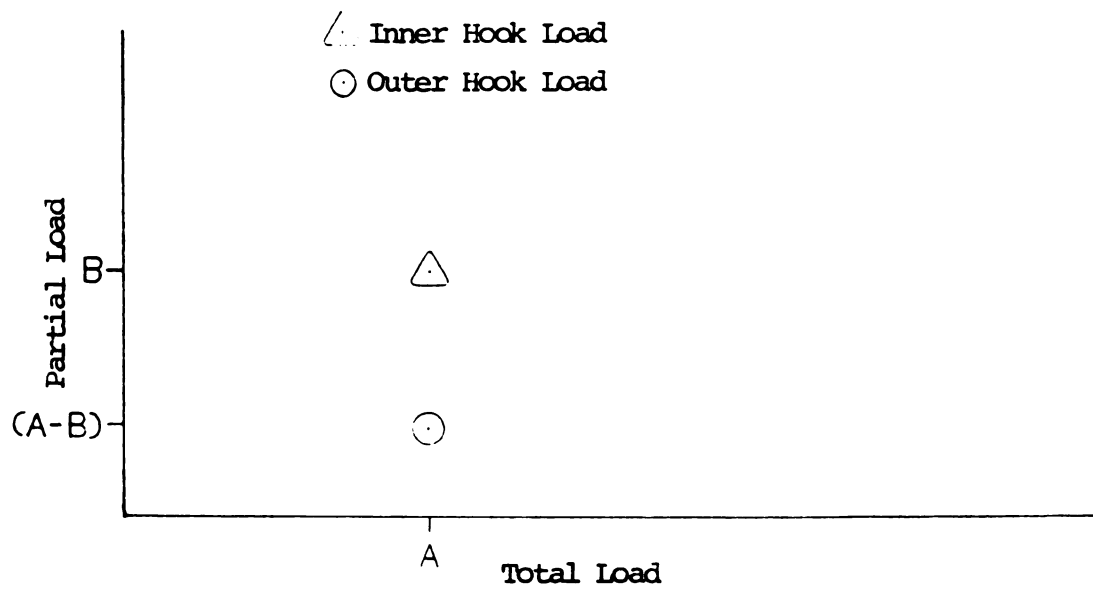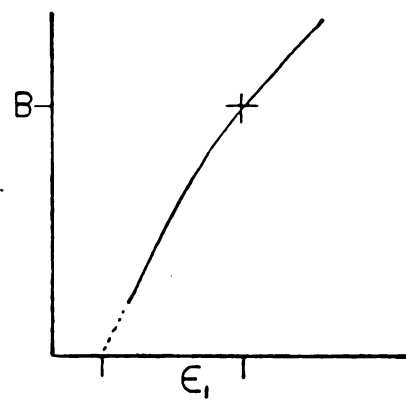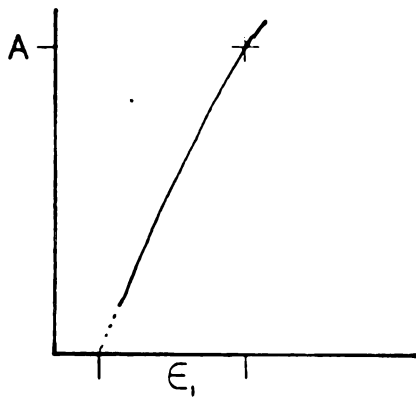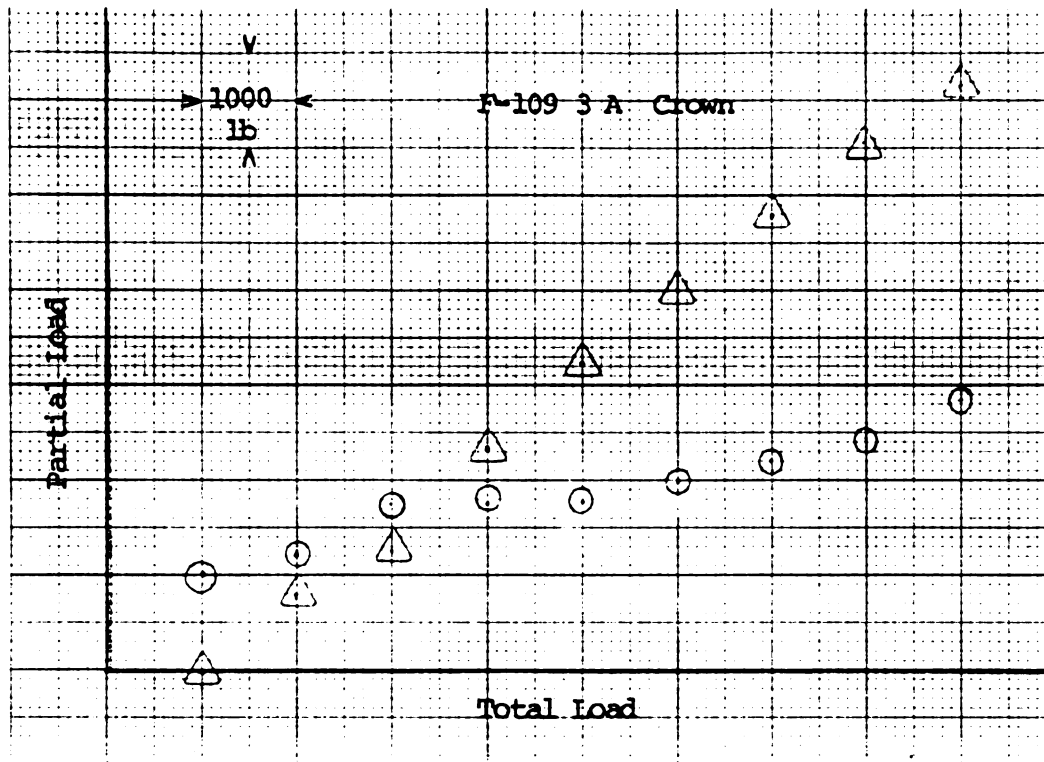
Inner Hook Load vs Strain Data

Figure 21   Load Split Determination
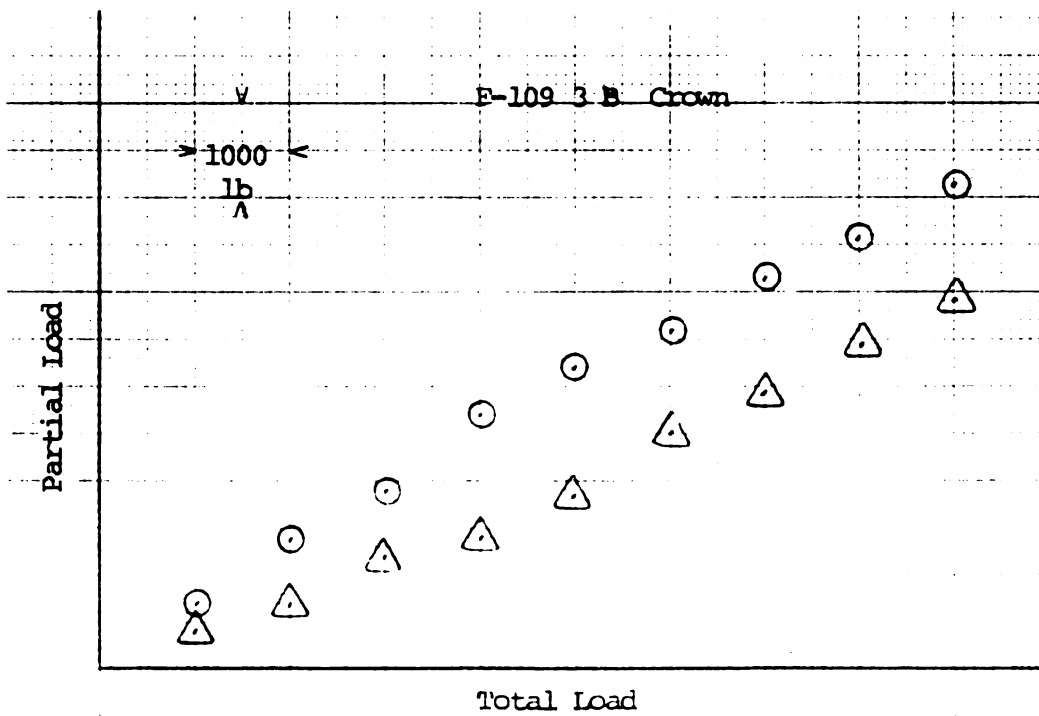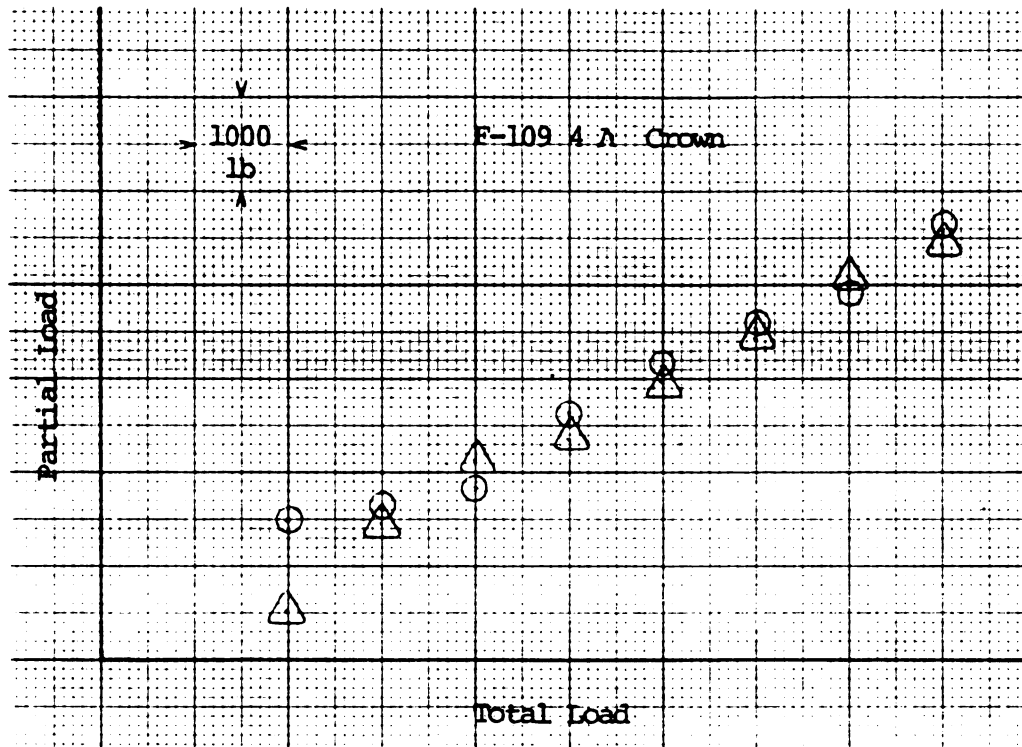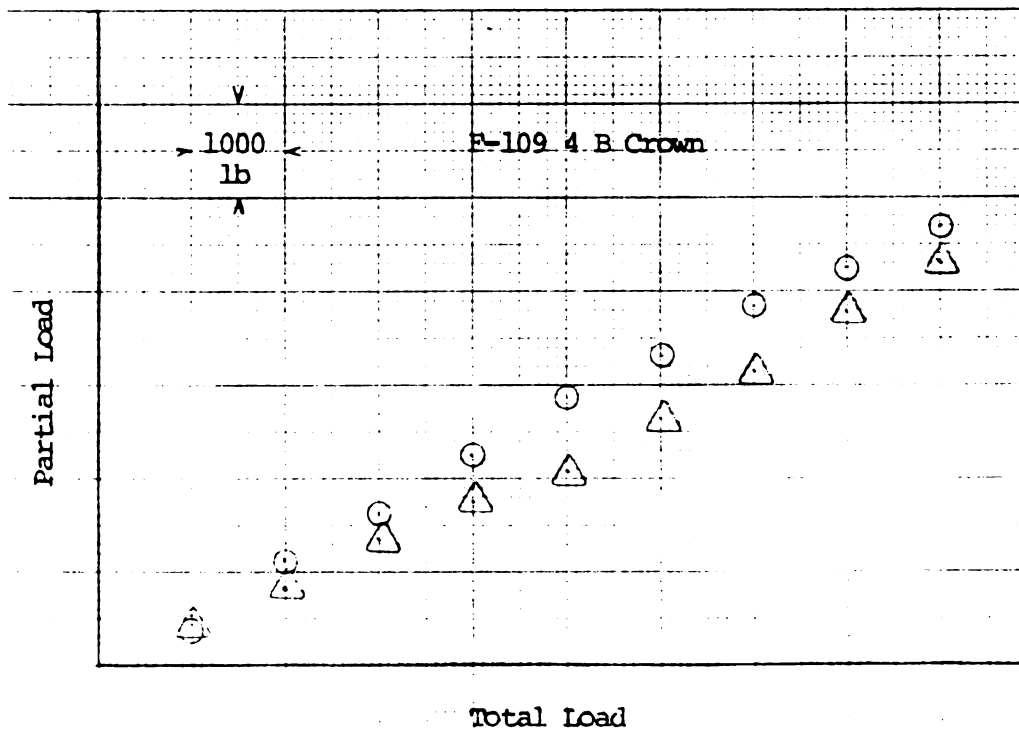
△ Inner Hook Load   ◯ Outer Hook Load

Figure 22   Load Split Data

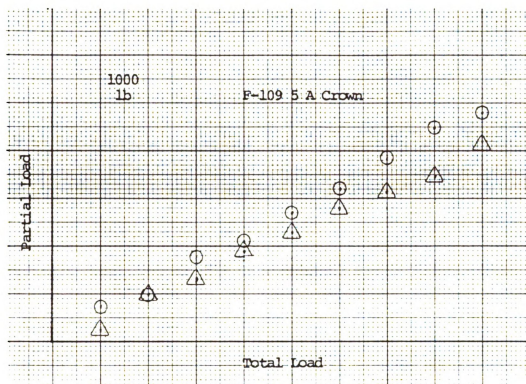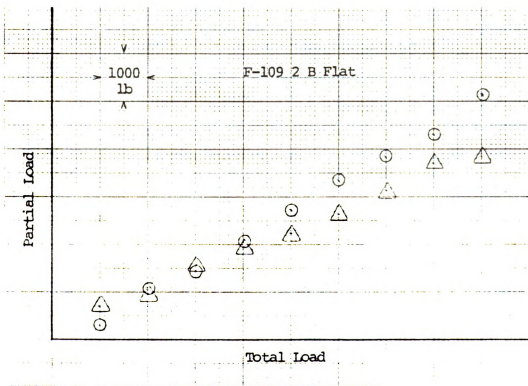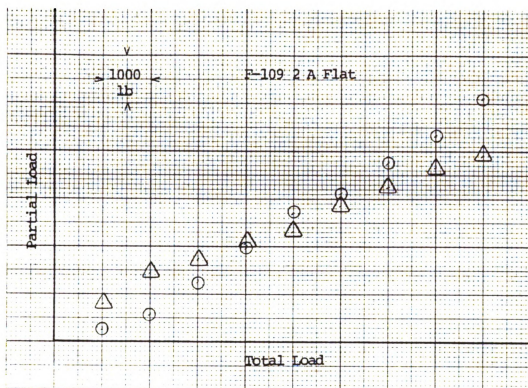△ Inner Hook Load   ◯ Outer Hook Load

Figure 23   Load Split Data

Figure 24   Load Split Data

Figure 25   Load Split Data

F-109 4 A Flat

Partial Load

Total Load
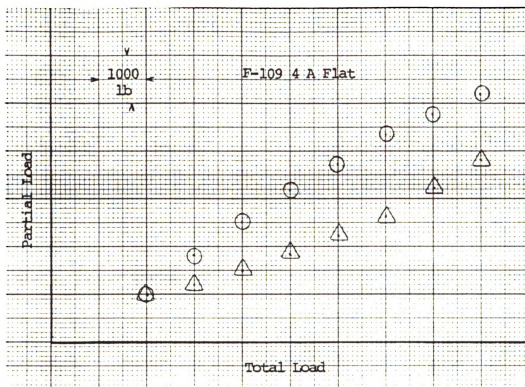
△ Inner Hook Loads   ◯ Outer Hook Loads

F-109 4 B Flat

Partial Load

Total Load

Figure 26   Load Split Data
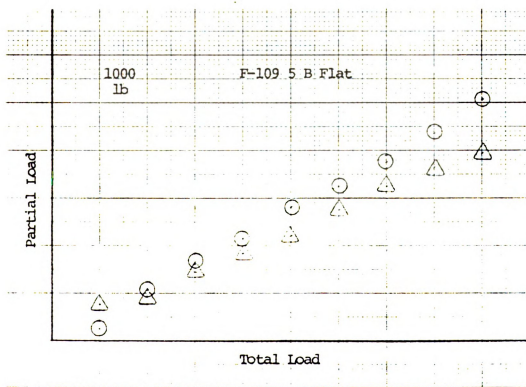
Figure 27   Load Split Data

fillet strains due to the load carried by the inner hooks were determined from the corresponding partial fixture data. The calculated load carried by the outer hooks was compared to the partial fixture data taken when only the outer hooks were loaded. A strain in the outer fillet due to the load on the outer hooks was determined. The sum of these two calculated strains were compared to the actual outer fillet strain. Based on the above calculations the principle of super-position did not hold for strains in the outer fillet.

The data produced by the preceeding process is shown in Figures 29-34.

Loads Applied at Arrows
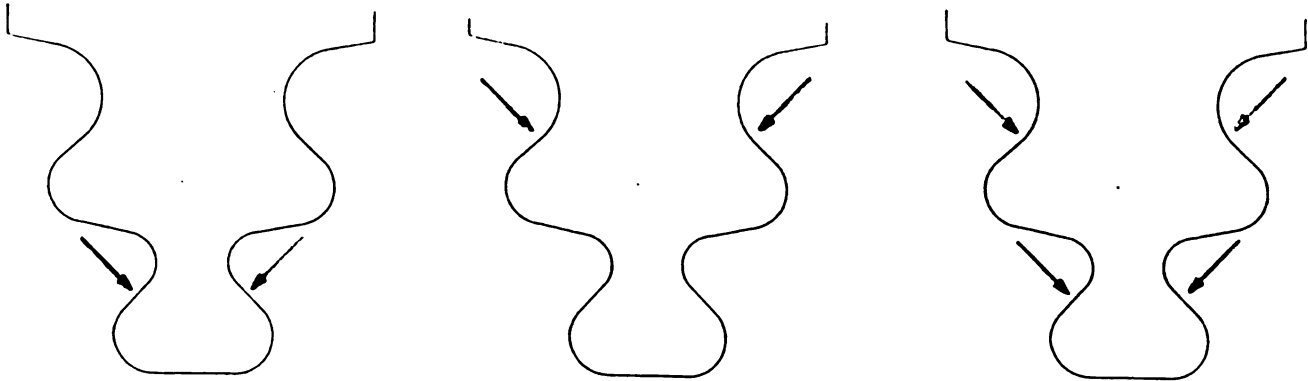
Outer Hook Load vs Strain Data
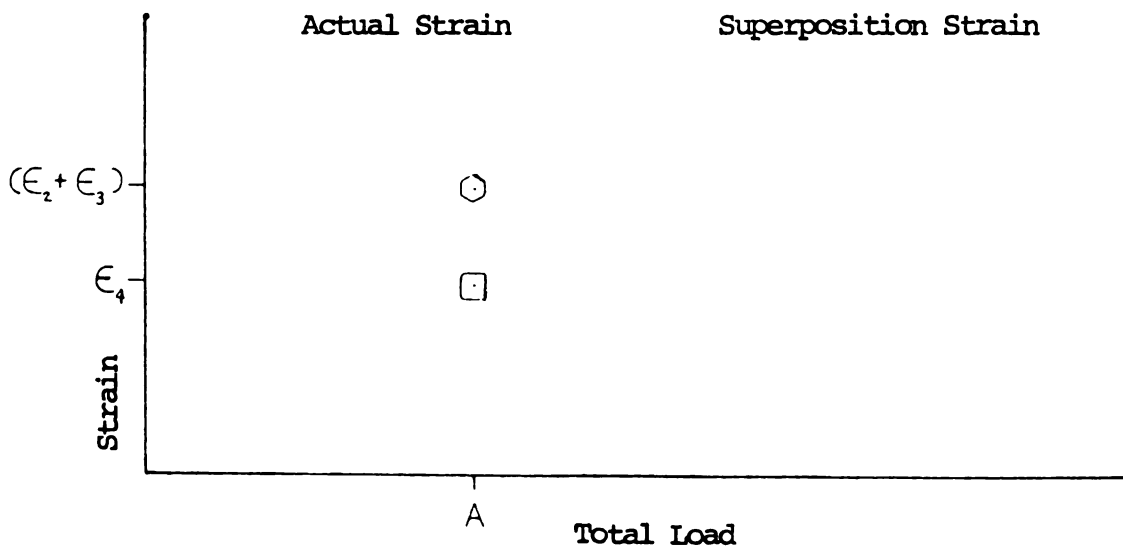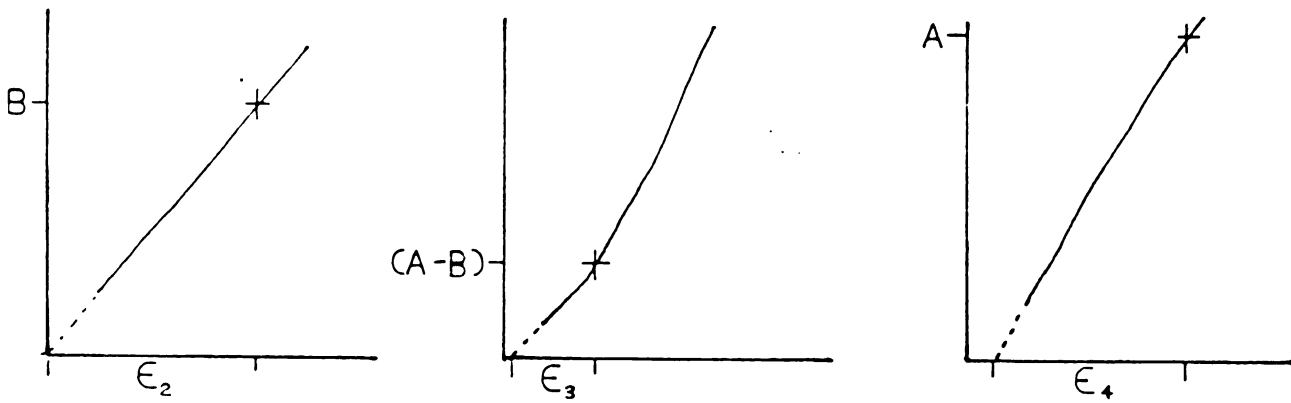
Figure 28   Superposition Determination
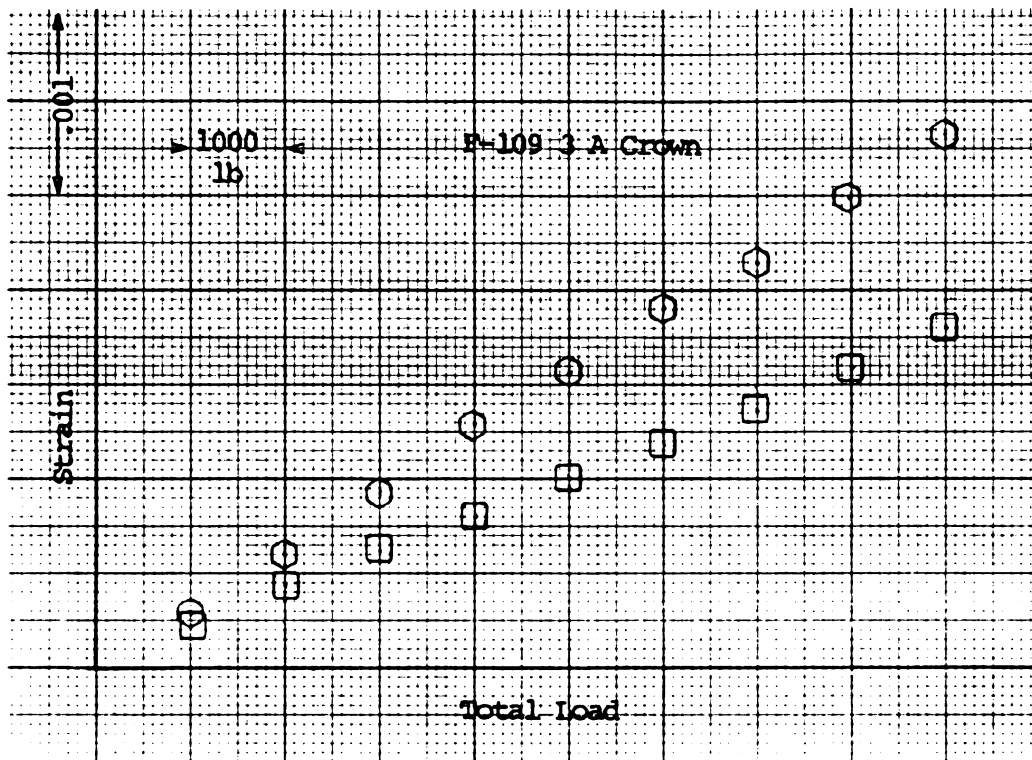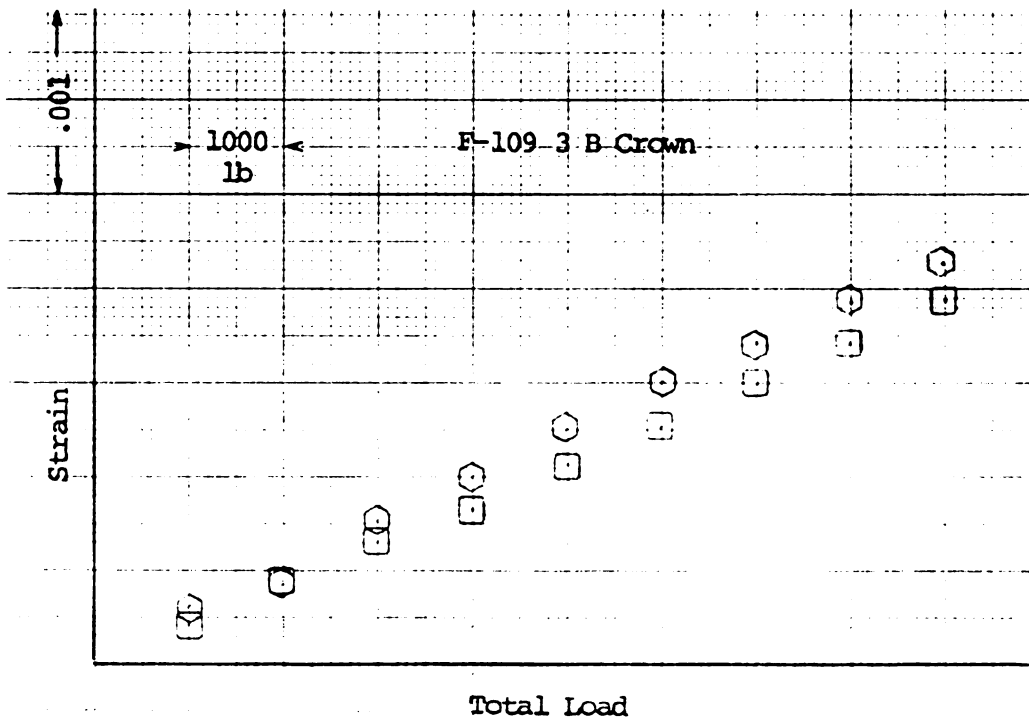
Figure 29   Superposition Data
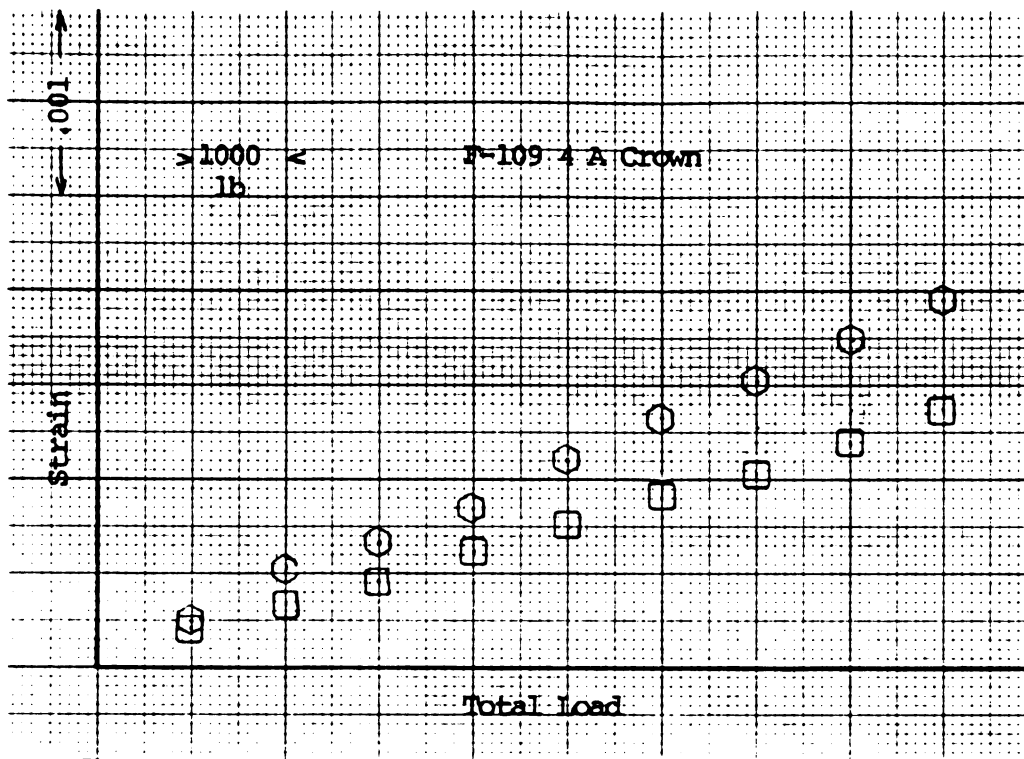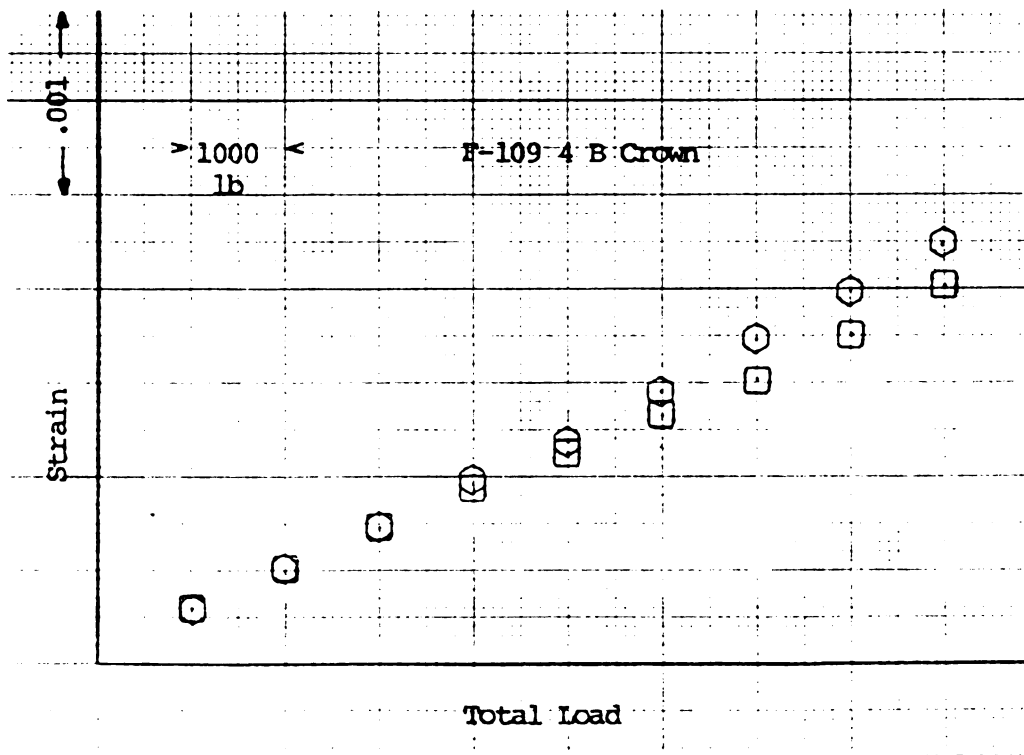
Figure 30   Superposition Data
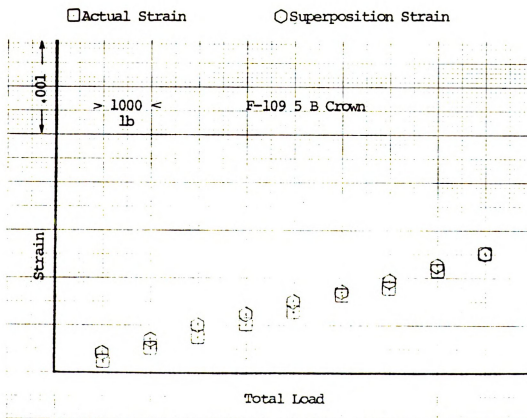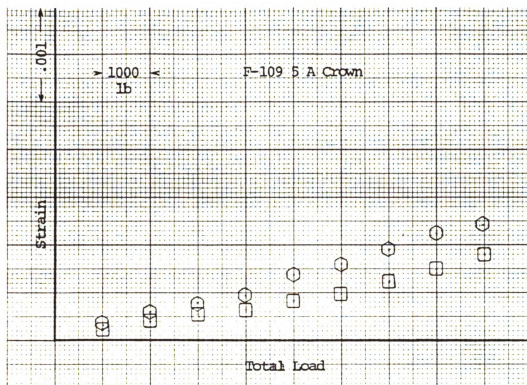
Figure 31   Superposition Data
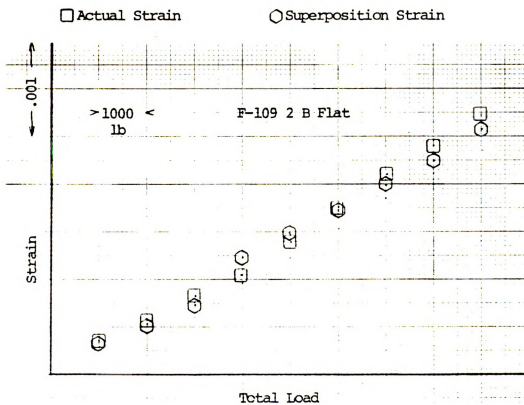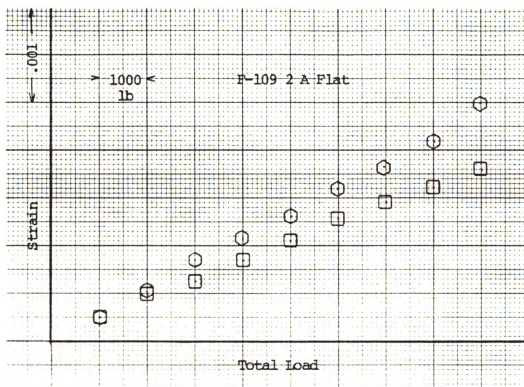
Figure 32   Superposition Data
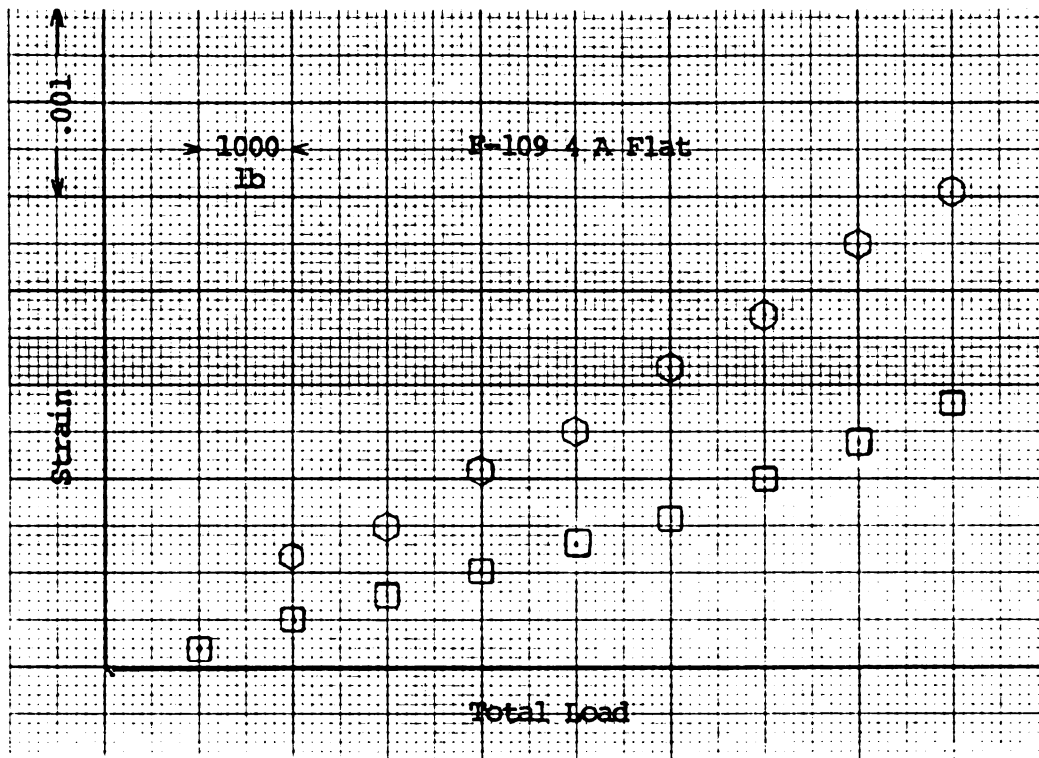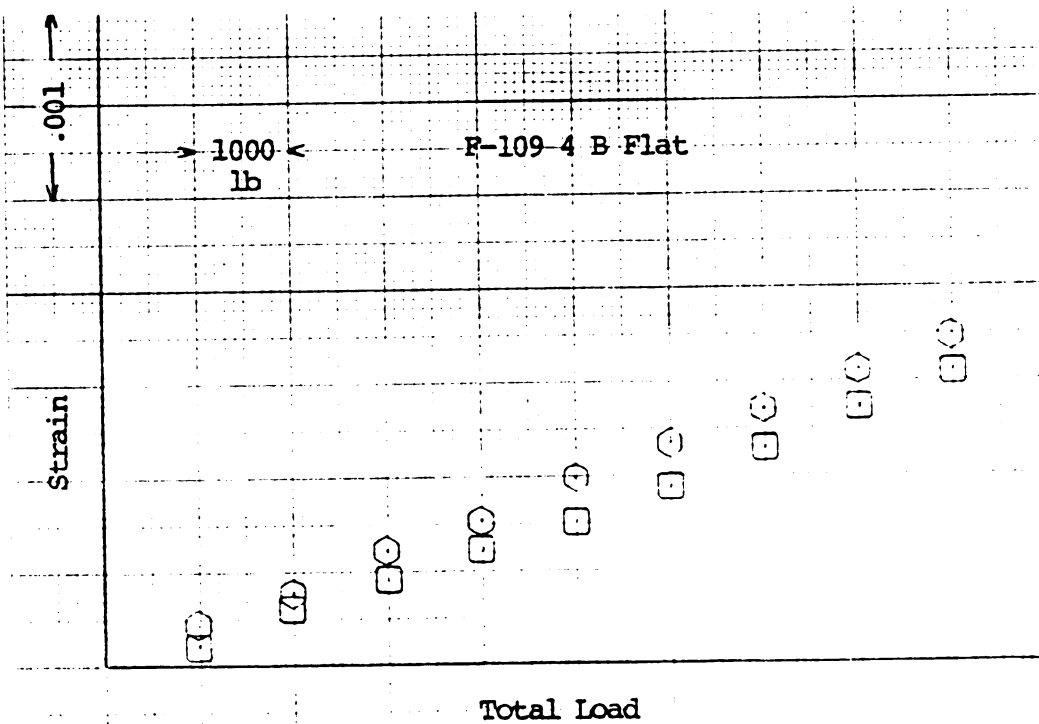
Figure 33   Superposition Data
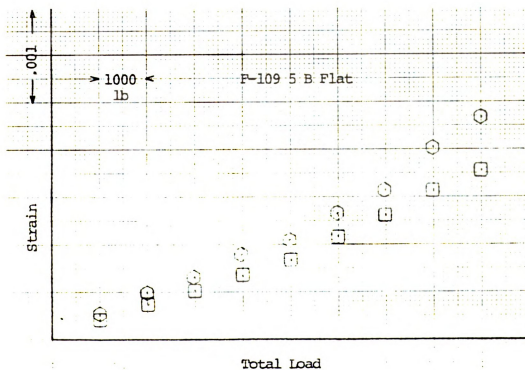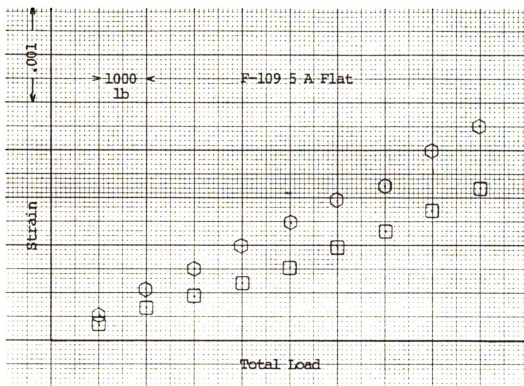
Figure 34   Superposition Data

CHAPTER 6

SPECIMEN ANALYSES

6.1 General Description

The two tang fir tree test specimens and loading fixtures to simulate the turbine disk were provided by Garrett Turbine Engine Company. The fir tree specimens are made of directionally solidified MAR 247, and the loading fixtures are Astroloy. Diagrams and specifications of the specimens and fixtures are contained in Figures 35 and 36. The two test specimen geometries are identical with the exception of the load bearing surfaces. The flat geometry specimens have plannar load bearing surfaces, while the crowned specimens have load bearing surfaces that are sections of a large radius circle as noted in the specifica-tions. The specimens and test fixtures are asymmetric about the Y axis. The reason for the assymetry is to provide an extended shoulder of supporting material for the trailing edge of the turbine blade as shown in Figure 37. The load bearing geometry of the loading fixtures had to accommodate the test specimens, and is necessarily axymmetrical too. The hooks on the fir tree, however are symmetrical.

Stresses in the blade attachment can be considered to result from two superimposed stress fields. Tensile
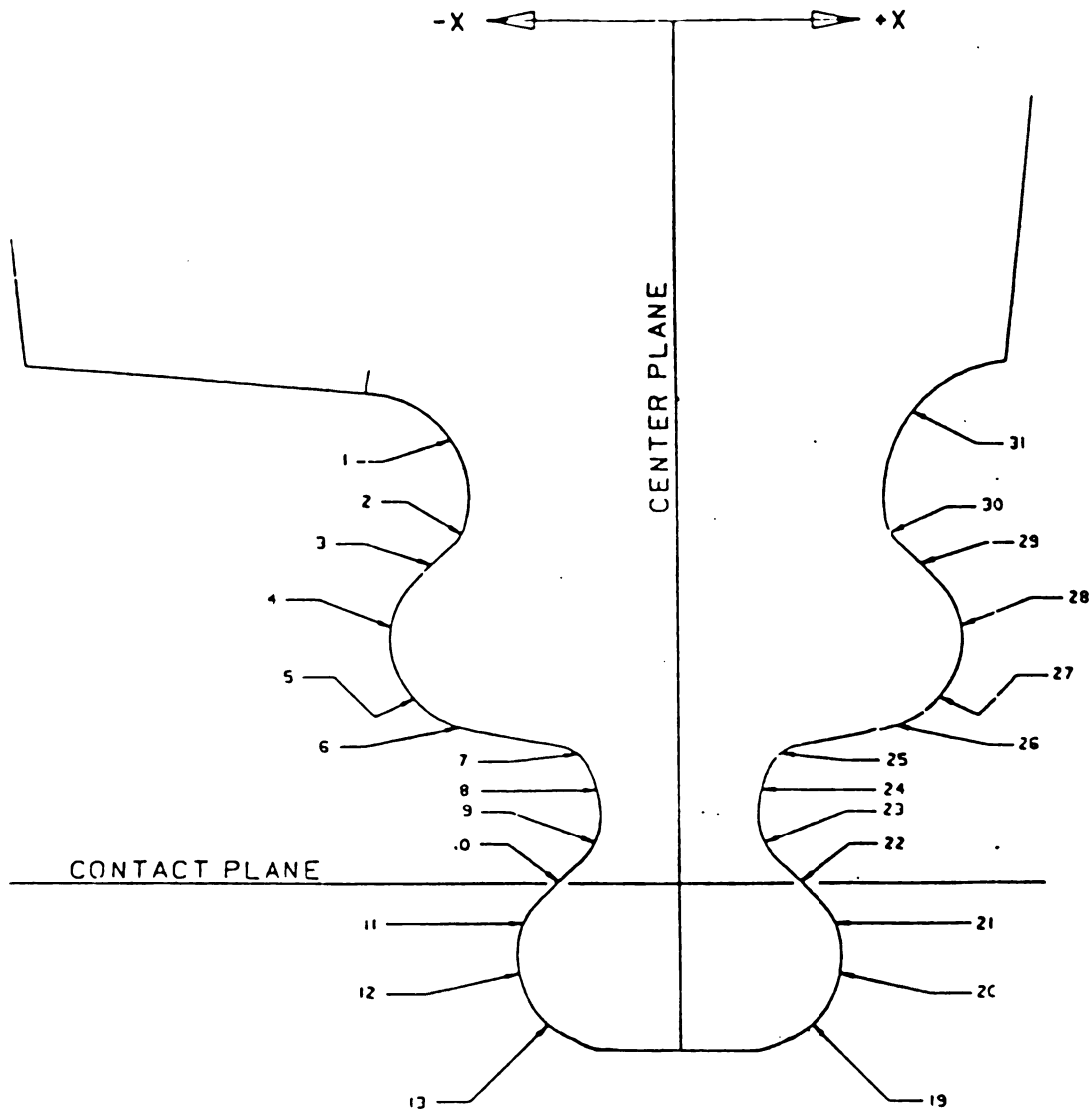
RADIUS NUMBER	-X- CENTER PLANE	-Y- CONTACT PLANE	RADIUS	TOLERANCE BAND INITIAL	FINAL
	-0.2747	0.2950		0.0030	0.0030
1	-0.1769	0.2262	0.0500	0.0030	0.0030
2	-0.1539	0.2263	0.0370	0.0030	0.0010
3	0.0712	-0.0313	0.3050	0.0010	0.0010
4	-0.1200	0.1436	0.0460	0.0010	0.0030
5	-0.1097	0.1475	0.0570	0.0030	0.0030
6	-0.1039	0.1347	0.0751	0.0030	0.0030
7	-0.0725	0.0599	0.0220	0.0030	0.0030
8	-0.1107	0.0403	0.0650	0.0030	0.0030
9	-0.0827	0.0401	0.0370	0.0030	0.0010
	-0.0714	-0.0000		0.0010	0.0010
10	0.1442	-0.2157	0.3049	0.0010	0.0010
11	-0.0537	-0.0395	0.0400	0.0010	0.0030
12	-0.0338	-0.0413	0.0600	0.0030	0.0030
13	-0.0471	-0.0483	0.0450	0.0030	0.0030
19	0.0471	-0.0483	0.0450	0.0030	0.0030
20	0.0338	-0.0413	0.0600	0.0030	0.0030
21	0.0537	-0.0395	0.0400	0.0030	0.0010
22	-0.1442	-0.2157	0.3049	0.0010	0.0010
	0.0714	0.0000		0.0010	0.0010
23	0.0827	0.0401	0.0370	0.0010	0.0030
24	0.1107	0.0403	0.0650	0.0030	0.0030
25	0.0725	0.0599	0.0220	0.0030	0.0030
26	0.1039	0.1647	0.0751	0.0030	0.0030
27	0.1097	0.1470	0.0570	0.0030	0.0030
28	0.1200	0.1436	0.0460	0.0030	0.0030
29	-0.0712	-0.0313	0.3050	0.0010	0.0010
30	0.1542	0.2261	0.0370	0.0010	0.0030
31	0.1971	0.2254	0.0800	0.0030	0.0010

3, 10, 22, 29 on
Crown Specimens Only

Figure 35   Specimen Specifications
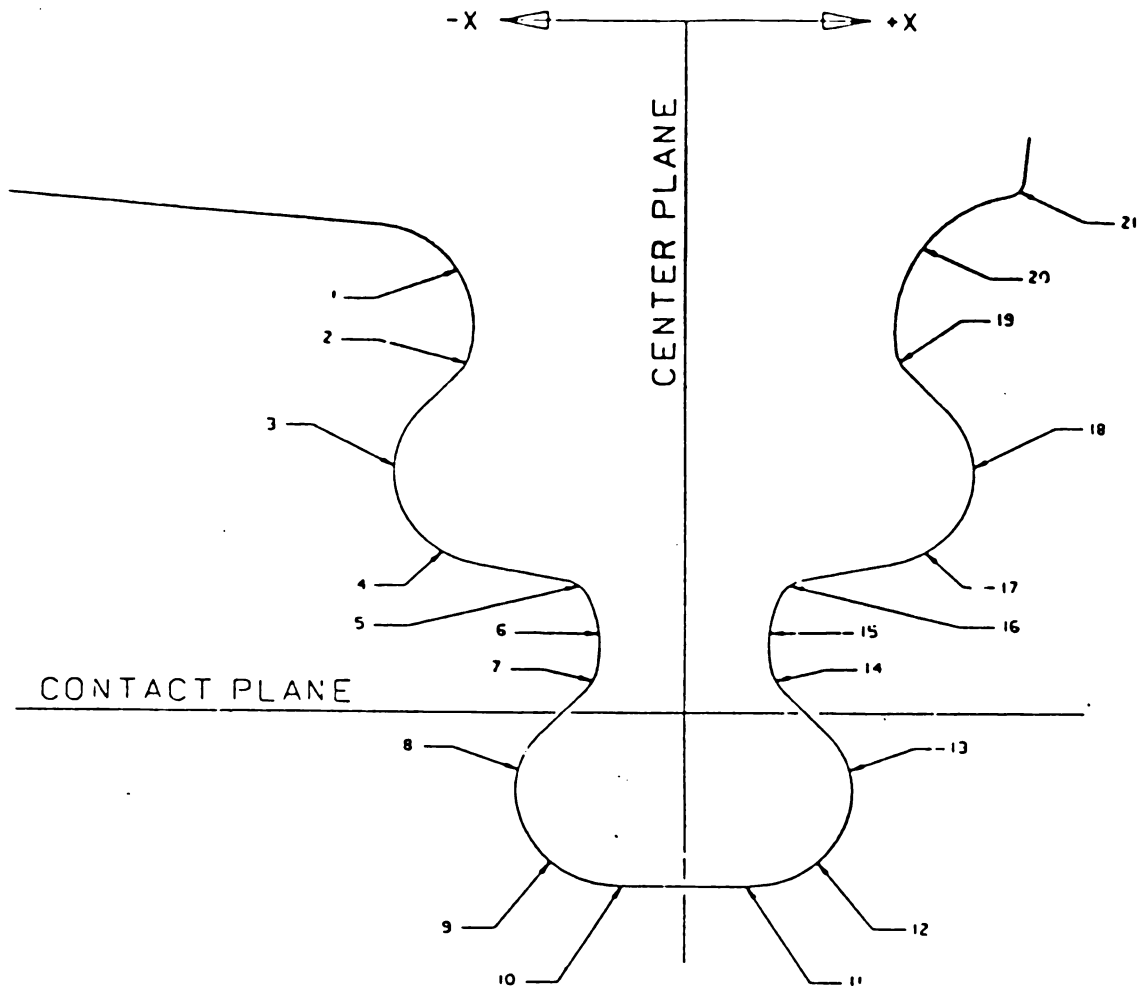
RADIUS NUMBER	-X- CENTER PLANE	-Y- CONTACT PLANE	RADIUS	TOLERANCE BAND	
				INITIAL	FINAL
1	-0.2878	0.2921	0.0580	0.0030	0.0030
	-0.1773	0.2242		0.0030	0.0030
2	-0.1563	0.2245	0.0370	0.0030	0.0010
3	-0.1188	0.1398	0.0500	0.0010	0.0030
4	-0.1111	0.1461	0.0600	0.0030	0.0030
5	-0.0724	0.0598	0.0180	0.0030	0.0030
6	-0.1148	0.0396	0.0650	0.0030	0.0030
7	-0.0785	0.0324	0.0280	0.0030	0.0010
	-0.0714	-0.0000		0.0010	0.0010
8	-0.0521	-0.0456	0.0460	0.0010	0.0030
9	-0.0409	-0.0428	0.0575	0.0030	0.0030
10	-0.0263	0.1005	0.2015	0.0030	0.0030
11	0.0263	0.1005	0.2015	0.0030	0.0030
12	0.0409	-0.0428	0.0575	0.0030	0.0030
13	0.0521	-0.0156	0.0460	0.0030	0.0010
	0.0714	-0.0000		0.0010	0.0010
14	0.0785	0.0324	0.0280	0.0010	0.0030
15	0.1148	0.0346	0.0650	0.0030	0.3030
16	0.0724	0.0598	0.0180	0.0030	0.0030
17	0.1111	0.1461	0.0600	0.0030	0.0030
18	0.1188	0.1398	0.0500	0.0030	0.0010
19	0.1568	0.2241	0.0370	0.0030	0.0030
20	0.1999	0.2223	0.0792	0.0030	0.0030
21	0.1878	0.3108	0.0100	0.0030	0.0030

Figure 36   Fixture Specifications
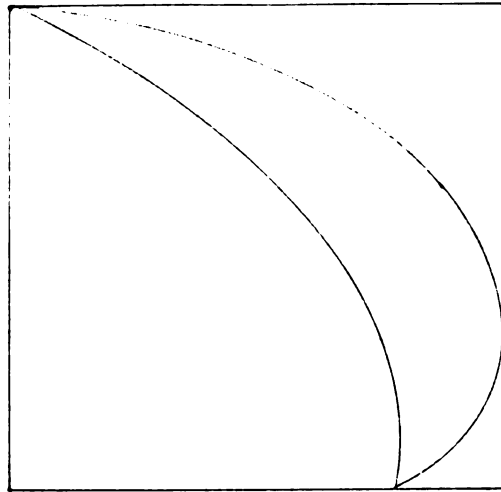
Top View
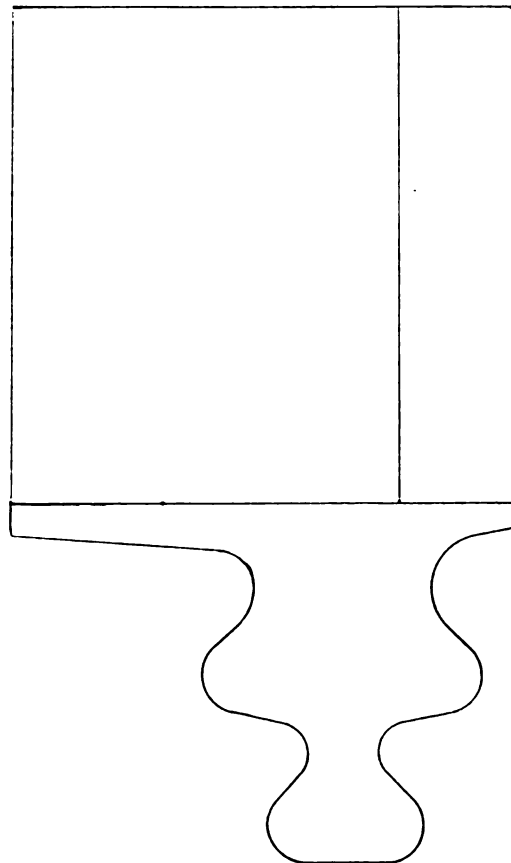
Front View

Figure 37   Specimen Asymmetry

stresses in the neck fillet region are due to the notches between the tangs. Another stress field arises from the bending of the tangs themselves. The neck stresses are expected to be greatest in the narrowest cross secton of the fillet, and the tang bending stresses are greatest where the tang joins the neck. The total stress anywhere in the attachment is a combination of the two fields.

6.2 Photoelastic Analyses

Photoelastic studies and data compiled by Heywood provide equations for the analysis of the stress in turbine blade attachments (12). The mathematics are simplified by the fact that the specimens are to be loaded in tension only. Thus the bending and twisting moments due to the aerodynamic loads on an actual turbine blade are not present. The equations are empirical in nature and were derived to give the best agreement with actual test results. Angular values used in the computations were calculated from the provided specimen dimensions. Distances that could not be easily calculated were measured on large scale drawings. For simplification of the initial problem, it was assumed that the load on the specimens was equally split between all four load bearing surfaces.

Neck stress concentrations were calculated from formula [6], with the paramteres as defined in Figure 38.

$$K_T = 1 + [\frac{1}{.8+5.6(h/a)} \cdot \frac{h}{R}]^{.65} [1 - (\frac{N-\epsilon}{180-\epsilon})^{1+2.4 \sqrt{R/h}}] \quad [6]$$
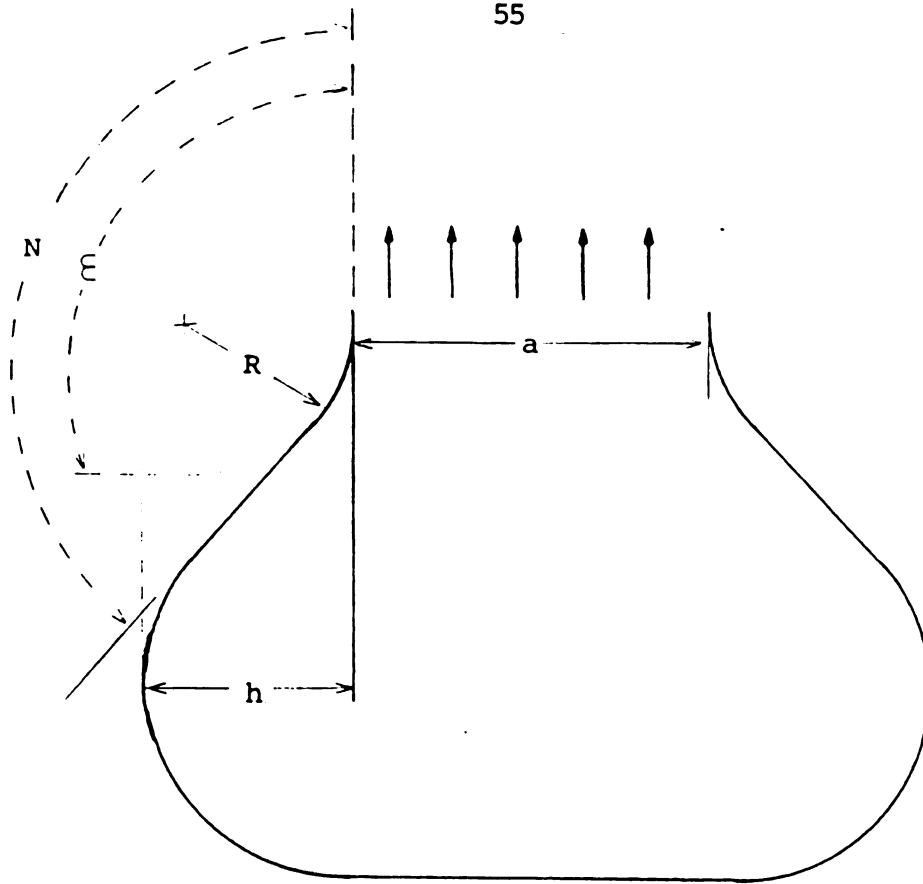
Figure 38   Neck Stress Parameters
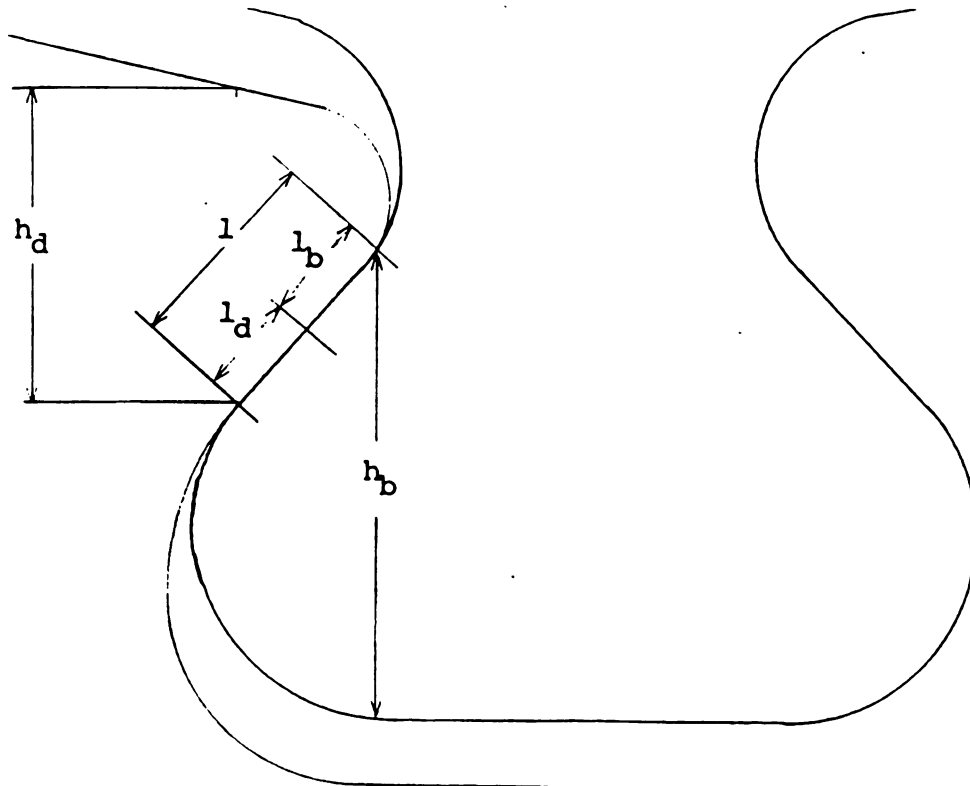
Figure 39   Point Load Resolution

When these calculations were carried out for both inner and outer paires of hooks, the stress concentration factors were:

K_T (inner hooks) = 1.44 K_T (outer hooks) = 1.67

These stress concentration factors combined with the assumed equal distribution of load yield maximum neck stresses of:

σ (inner fillet) = 116 ksi σ (outer fillet) = 104 ksi

The parameters used in the above calculation are the same for both flat and crowned specimens.

To compute the stresses associated with bending of the tangs themselves, the distributed load along the load bearing surface must be resolved to a point load. For the crowned geometry, this is simply the middle of the load bearing surface. For the flat specimens, however, the load location must be computed using the following formula [7] and Figure 39.

$$lb = \frac{1}{1 + \sqrt{\frac{Ed}{Eb}\left(\frac{hd}{hb}\right)^3}} \quad , \quad ld = \frac{1}{1 + \sqrt{\frac{Eb}{Ed}\left(\frac{hb}{hd}\right)^3}} \quad , \quad l_b + l_d + 1 \tag{7}$$

Where E_b and E_d refer to the modulus of the blade and disk material, respectively. The modulus of the blade material was measured on a test specimen under tensile load with interferometric equipment. The modulus for astrology, the fixture material, was provided by Garrett. The length l was computed from the specimen and fixture specifications. For nominal tolerances in the flat geometry case, the resultant

center | line
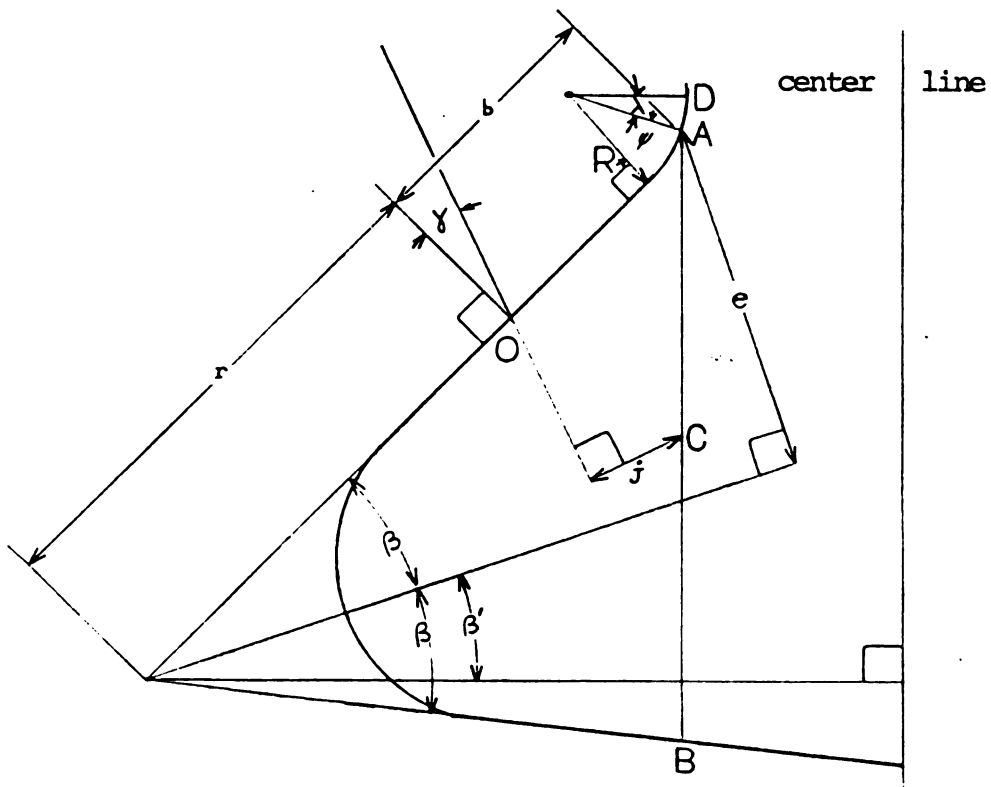
Figure 40   Inner Hook Stress Parameters

loads act at the following points on the load bearing surfaces of the hooks.

inner hook l_b = .0155 in   outer hook l_b = .0135 in

The inner hook stresses are computed using formula [8] with the dimensions and angles from Figure 40.

$$\sigma_t = \left(\frac{1.5j}{e^2} + \frac{0.36}{\sqrt{be}} \left(1 + \frac{1}{4} \sin \gamma \right) \right) \frac{w}{\cos (\beta + \beta' - \gamma)} \qquad [8]$$

An assumed frictional coefficient of 1/3 between the blade and disk yields an angle of 20 degrees for γ, and Heywood specifies ψ as 30 degrees for the inner hook of multiple projection fir trees. Completing these calculations yield nominal stresses at point A of:

In a similar manner, the stress for the outer set of tangs is computed using the same formula and Figure 41, with ψ equal to five degrees.

A hook stress concentration factor formula [9], empirically derived by Heywood is applied to the calculated hook stresses,

$$K_t = 1 + .26 \left(\frac{e}{R} \right)^{.7} \qquad [9]$$

This yields hook stresses of:

Flat Geometry	Crowned Geometry
inner hooks 71,000 psi	71,700 psi
outer hooks 120,000 psi	120,000 psi

This coincides well with the partial fixture data taken at the outer set of hooks. The mean stress at the outer fillet was the same when the inner hooks were loaded and when the outer hooks were loaded. Higher maximum strains
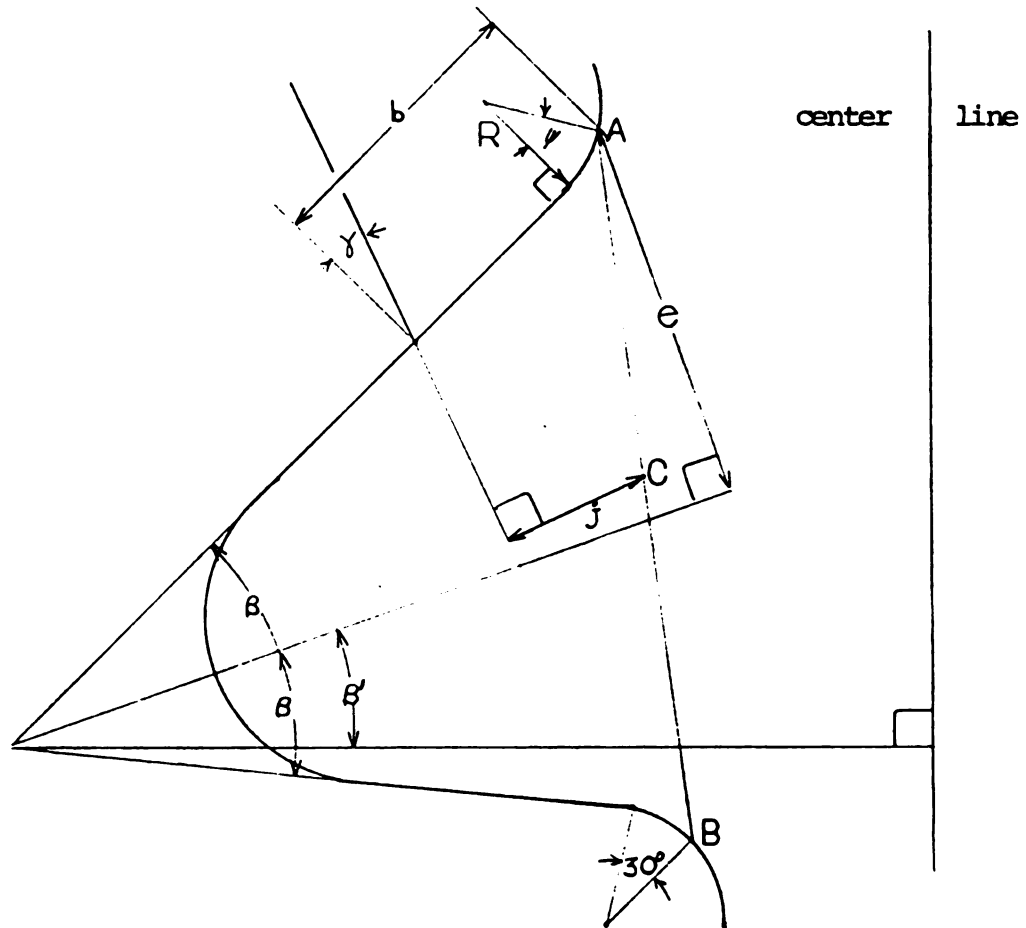
Figure 41   Outer Hook Stress Parameters

were recorded in the outer fillet when the outer hooks carried the load.

6.3 Finite Element Analysis

Finite element data generated by Garrett (3 and 4) produced the stresses resulting from the superimposed neck and hook stress fields as shown in Figures 42 and 43. The data were based on a maximum tensile load of 11,750 pounds and a frictional coefficient of 1/3. The Garrett data included stress plots for nominal and 1/2 worst case tolerances, with a friction coefficient of 1/3. In the two finite element studies, the radial or Y direction stresses and the principal stresses are almost the same in the fillet region.

The similar nature of the separate stress plots indicate that the principal stress in the neck region runs in the radial direction parallel to the Y axis of the specimen.

Figure 44 shows the comparisons between the stresses generated by the photoelastic analyses and the finite element stresses. Hook stresses from the photoelastic equations, however do not fit the Garrett finite element data. Anisotropy of the specimen material is not accounted for in the photoelastic equations.
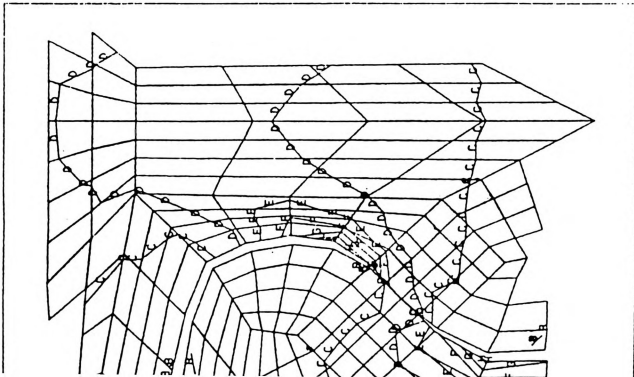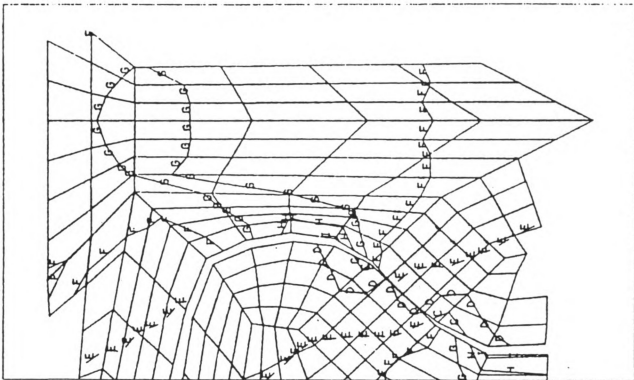
Figure 42   Finite Element Analysis
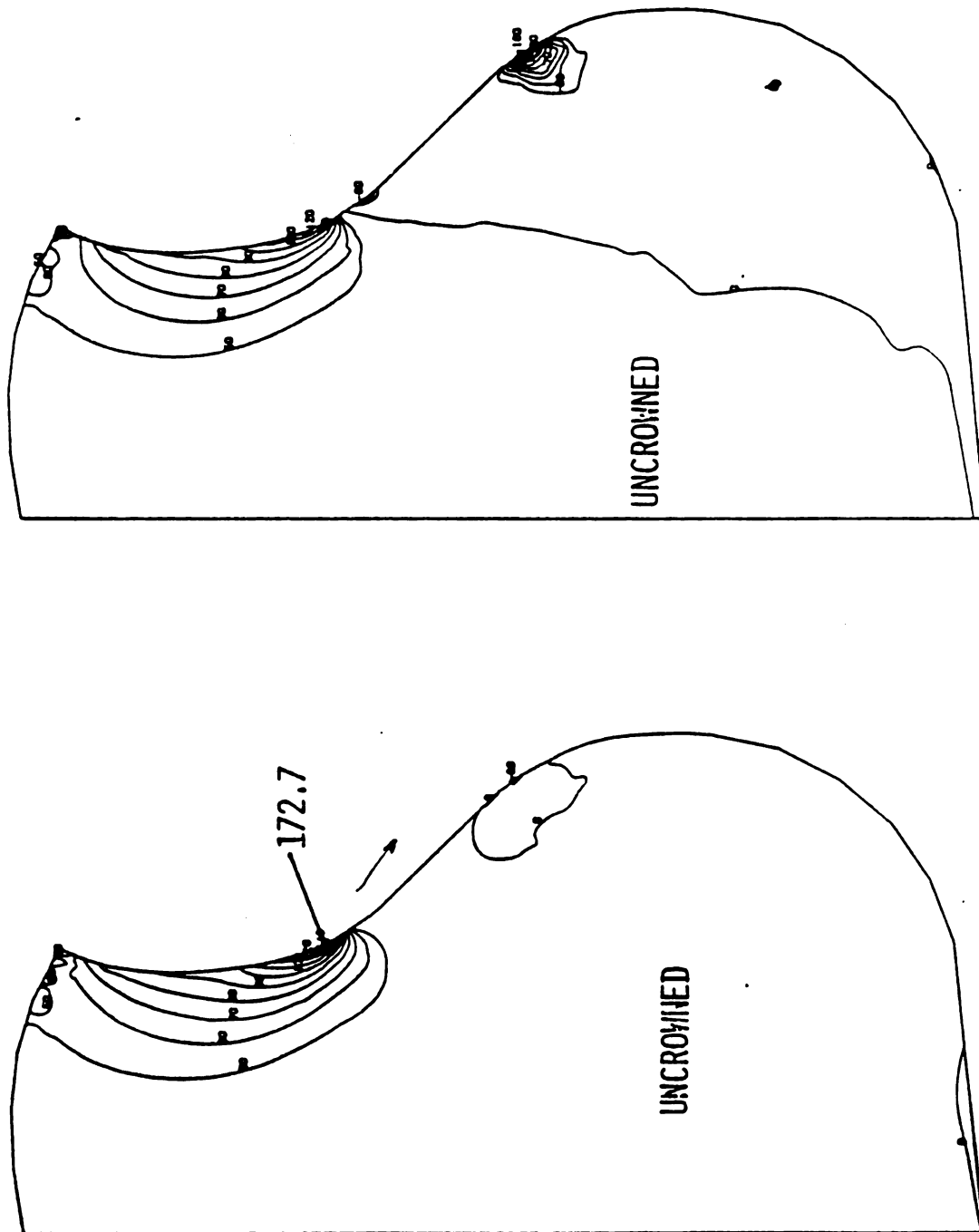
Figure 43   Finite Element Analysis

	Neck Stresses		Hook Stresses	
	Inner	Outer	Inner	Outer
Photoelastic Computations				
Crowned	116 ksi	104 ksi	72 ksi	120 ksi
Flat	116 ksi	104 ksi	71 ksi	120 ksi
Finite Element Method #1				
Figure 42	100 ksi	120 ksi	138 ksi	280 ksi
Finite Element Method #2				
Figure 43				
Crowned	95 ksi		183 ksi	
Flat	100 ksi		237 ksi	

Figure 44   Stress Comparisions

CONCLUSIONS

Characterization of the effects due to machining tolerances produced two very noticeable phenomena. First, compressive strains were recorded in the inner fillet region. These compressive strains result from bending moments caused by the slight mismatch between the fir tree and the loading fixutre. Nearly 2/3 of the tested specimens showed some bending in the inner fillet. Cyclic strain data indicated that slippage of contact surfaces was occuring as load changed.

Load split determinations were performed. For 11 of the 12 data sets, a relatively even load split between the inner and outer fillets was observed. With the load split data the principle of superposition of strain fields was tested. However, it did not hold for strains in the outer fillet region.

The photoelastic and finite element data agreed qualitatively with the measured strain distribution across the fillet region. When numerically compared to the photoelastic and finite element data, the actual surface strains were far below expected. This indicates that somewhere in the attachment, strains and stresses are higher than predicted.

APPENDIX 1

RIGID BODY MOTION EFFECTS ON THE ISG

1.1 Rigid Body Motion of the Specimen

During initial shakedown runs of the system to test the load train, ISG, recorders and controller, two significant and unforeseen complications were noted. First,because of the number and overall length of the load train components there was a comparatively large and easily visible amount of vertical motion of the specimen at high cyclic loads due to elastic deformation. During triangular wave loading from 580 to 11,750 pounds the vertical motion at the specimen was measured with a dial gauge at .050 inches, Figure 45.

In addition to the perceived vertical motion, the specimen shifted in the loading fixture causing a change in alignment of the fixture and specimen centerlines, Figure 46. This shifting resulted in an angular displacement between initially coincidental specimen and fixture axes. This displacement was measured from photographs at approximately 8 degrees.

These two factors have a considerable effect on the ability to produce accurate data with the ISG.
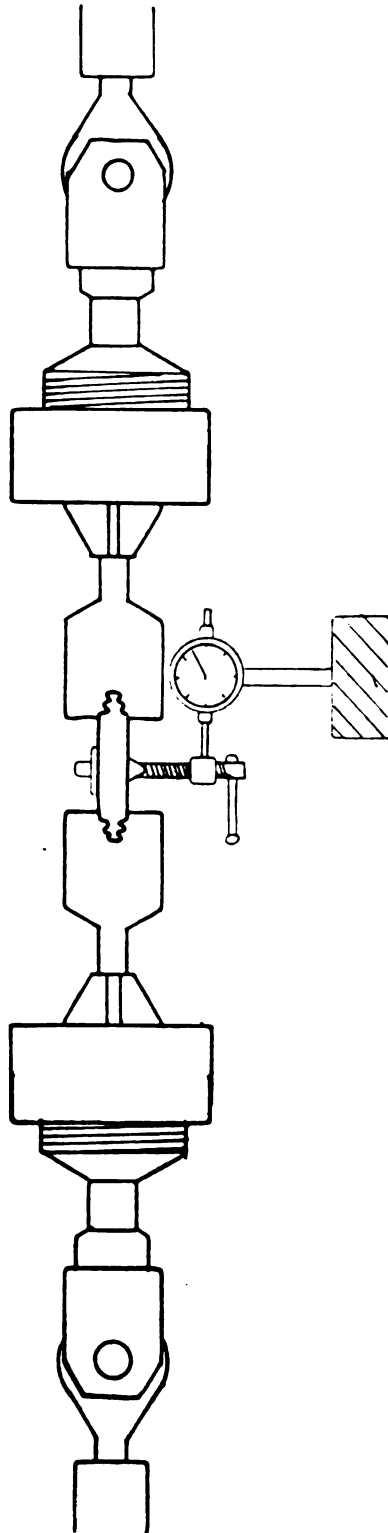
Figure 45   Specimen Vertical Motion
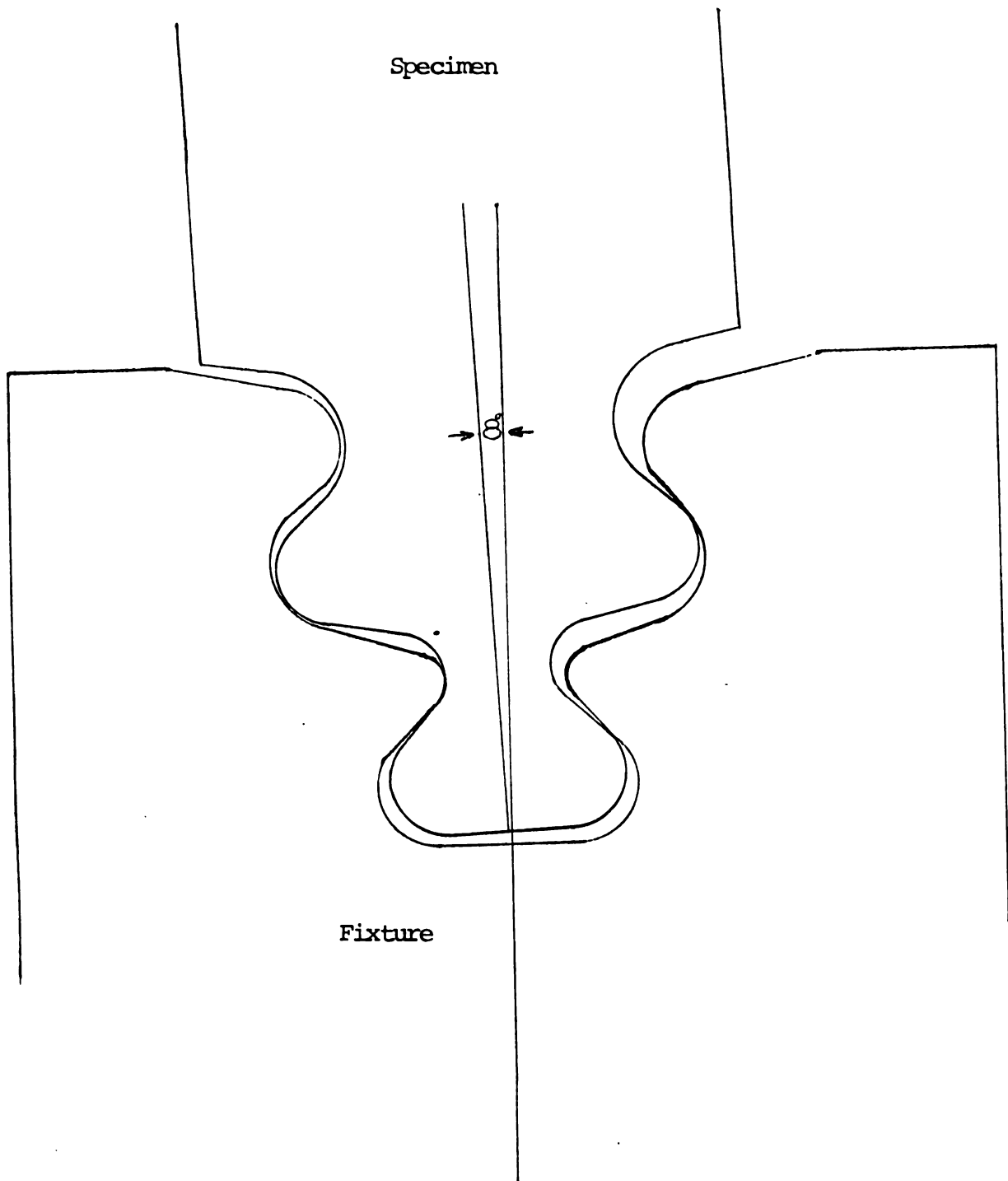
Specimen

δ

Fixture

Figure 46 Angular Displacement of Specimen and Fixture

1.2 Vertical Motion Effects on the ISG

The ISG measures strain by comparing the phase shift of two sets of interference fringe patterns produced by reflecting laser light from two pyramidal indents on the specimen surface. The ISG averages the phase shift of two sets of fringes and compares this to an initial value. This averaging allows the indents to translate along the same axis as the ISG without producing erroneous data. The laser used to illuminate the indentations on the specimen has a beam width of approximately 2 cm. During high load tests the indents would move out of the illuminated area and no data would be produced. Even at lower loads there would be considerable rigid body motion compared to the strains being measured. It had to be determined whether a loss in accuracy would result from the decreasing fringe pattern strength as the indents moved toward the edge of the laser illuminated area.

To evaluate this problem and determine the working range of the ISG, the following experiment was performed. A rigid bar was clamped to the base of the load train extending upward toward the specimen. At the same level as a test specimen, an indented specimen was clamped to the bar, Figure 47. The ISG was aligned on the clamped specimen and strain measurements were taken during various loading cycles. Because no loads were being applied to the clamped specimen, the ISG if operating correctly should show no strain in the specimen as long as sufficient signal strength
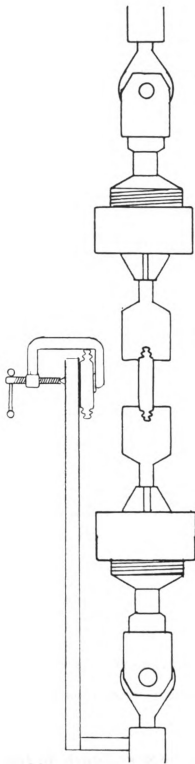
Figure 47   ISG Vertical Motion Test

was available. The clamped specimen was rigidly attached to the base of the load train, it underwent twice the vertical motion of the actual test specimen held by the fixtures. During cyclic test loads from 500 to 4500 pounds the ISG output remained linear and showed no strain through approximately 3/4 of the cycle. Some operator expertise was required to align and properly adjust the ISG. Due to operator experience there was a high degree of confidence that the data obtained was not adversely affected by vertical rigid body motion.

1.3 Angular Displacement Effects

In addition to vertical rigid body motion of the specimen, that the ISG can accommodate without loss of accuracy, there was the previously mentioned angular displacement. The ISG, however was not designed to handle angular deviations that would change the alignment of the indentations on the specimen in relation to the initial alignment axis. As shown in Figure 48 an angular displacement from the initial alignment would cause the fringe patterns on the face of the mirrors to shift slightly toward each other. This slight phase shift is interpreted as tension by the computer system. For large strains and very small displacement angles the effect might be negligible.

The estimated displacement angle measured during shakedown runs was eight degrees. The following calculation
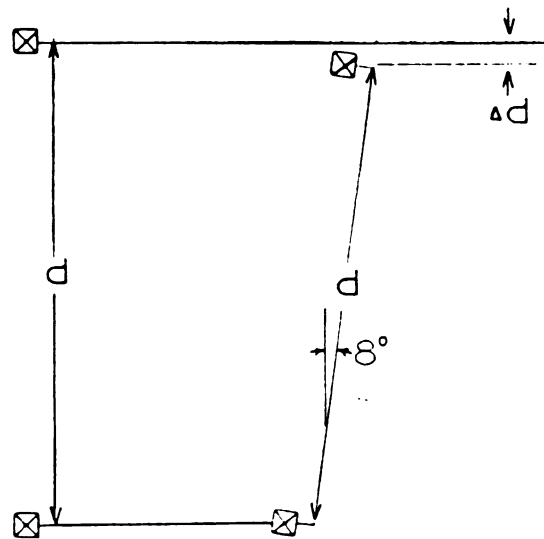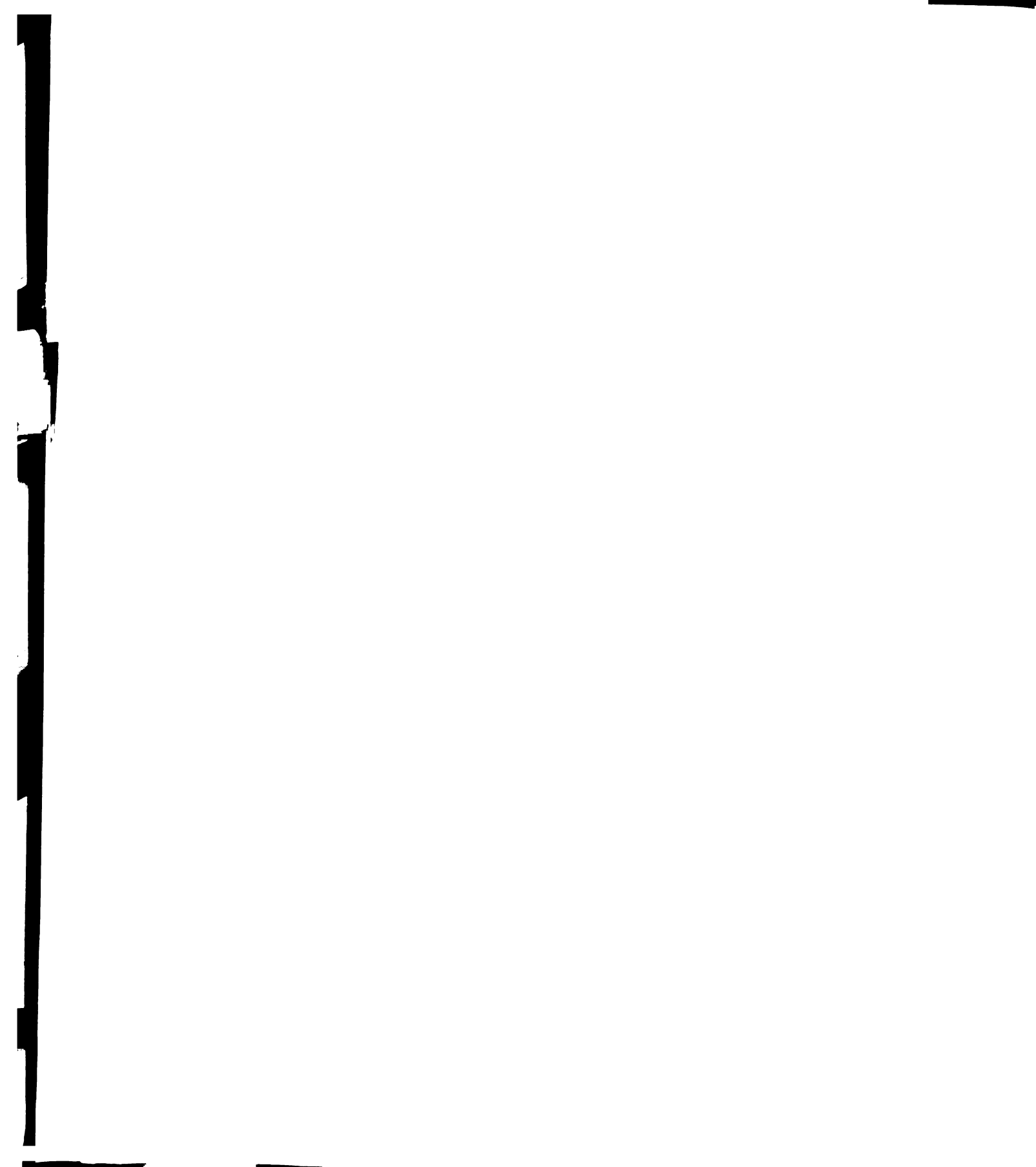
Figure 48   Angular Displacement Error

[10] shows that an angular displacement of only one degree would cause an indicated change in strain of

$$\text{strain} = \frac{\Delta d}{d} = \frac{d(1 - \cos 1°)}{d} = .00015 \qquad [10]$$

d = distance between indentations

This is a considerable error compared to the predicted and measured surface strains.

Also, as the angular displacement increases the sine wave signal generated by the mirror sweeping the fringe pattern past the slit on the face of the photomultiplier tube becomes distorted, Figure 49. This distortion results in an extreme loss of accuracy in the ISG data, especially as signal intensity is lost. Signal intensity decreases rapidly when the indents move along the edge of the laser illuminated area.

1.4 Rigid Body Motion Corrections

The distortion and loss of signal intensity were a compound problem. As the top of the sine wave becomes flatter, the computer has more trouble establishing the location of the greatest value of each peak. By tracking the phase shift of these peaks, the computer calculates the phase shift and the resulting strain. Loss of signal strength further flattens the sine wave and degrades the data.

The following procedure was used to obtain the indicated but not actually present strains caused by angular deviations from the ISG axis.
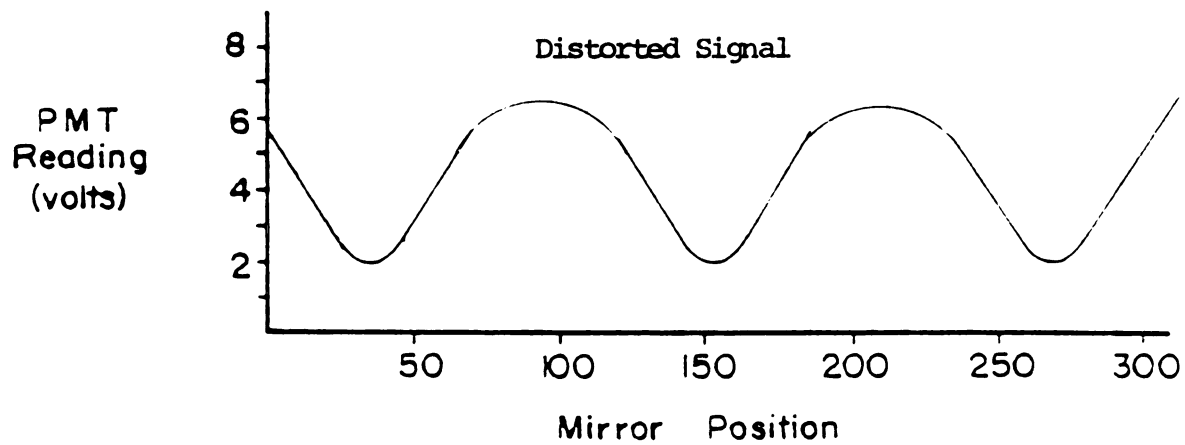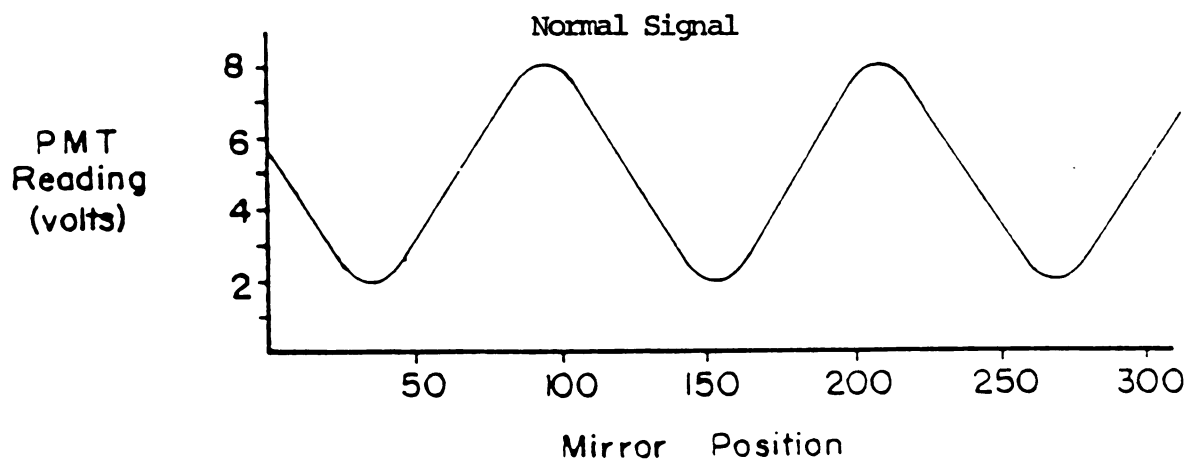
Figure 49   Signal Distortion

First the test specimen was placed in the fixtures and loaded to the median load of the test cycle. For high load runs this was 4750 pounds, while for partial fixture and fit characterization runs it was 2500 pounds. With the specimen under tension the ISG was carefully aligned. During allignment great care was taken to assure that the mirror axis and the axis of the fringe pattern concided. This effort was facilitated by the shape of the fringe patterns themselves. The interference patterns generated by the pyramidal indentations have an "Eiffel Tower" shape with an easily discernable axis.

On the test specimens all 12 sets of indentations were parallel to each other and had the same relationship to the axis of the specimen. This was ensured during the indentation process by holding the specimen in a special jig so there could be no motion but the horizontal and vertical translation of the micropositioning table.

After test data were gathered on a specimen, rigid body motion data was taken. A small indented block of material was attached with double sided tape to the indented face of the specimen away from any possible contact with the holding fixtures. The two sided tape would prevent any specimen strains from being transferred into the indented block. Additionally, it was assumed that the surface strains present in the test specimen would be small and evenly distributed enough that the block would not change orientation on the specimen during a loading cycle. No

No changes were made in the ISG position or orientation. The indented block was adjusted so that its fringe patterns lined up exactly on the ISG mirrors. Since no change had been made in ISG position, the alligned fringe patterns meant that the indentations on the block and the test specimen were parallel and both had the same relationship to the ISG. The test specimen was subjected to another loading cycle. This time however, the only data generated came from the motion of the indented block and not from actual strains. The data from the rigid body motion runs was subtracted from the specimen data runs to produce data free from rigid body motion error, Figure 50.

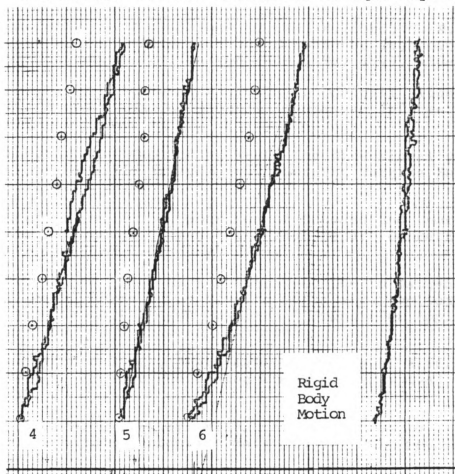O Indicates Data Points Corrected for Rigid Body Motion

Figure 50   Rigid Body Motion Correction

LIST OF REFERENCES

1. Signorelli, R. A., Glasgow, T. K., Halford, G. R. and Levine, S. R., "Materials and Structures Technology," NASA Conference Publication #2092, May 1979, 150-162.

2. Macke, H. J., "General Analysis of Dovetail Blade Attachments," General Electric Technical Information Series, December 1959.

3. Lucas, L. J., "Supporting Tests for Directionally Solidified Blade Attachments," Garrett Turbine Engine Co., 1984.

4. Denniston, W. E., "Comparison of Crowned and Uncrowned Blade Attachment Stress," Internal Report Garrett Turbine Engine Co., June, 1983.

5. Smith, J. O., Liu, C. K., "Stresses Due to Tangential and Normal Loads on an Elastic Solid with Application to some Contact Stress Problems," Journal of Applied Mechanics, June 1953, pp. 157-166.

6. Sokolnikoff, I. S., "Mathematical Theory of Elsticity," Robert E. Kreiger Publishing Company, Inc., 1983, pp. 24-55.

7. Durelli, A. J., Wiley, W. F., "Introduction to Photomechanics," Prentice Hall, Inc., 1957, pp. 220-231.

8. Sharpe, W. N., Jr., "The Interferometric Strain Gage," Experimental Mechanics 8, April 1968, pp. 164-170.

9. Sharpe, W. N., Jr., "Interferometric Surface Strain Measurement," International Journal of Non-Destructive Testing 3, 1971, pp. 51-76.

10. Sharpe, W. N., Jr., "A Short Gage-Length Optical Gage for Small Strain," Experimental Mechanics, 14, 1974, pp. 373-377.

11. Sharpe, W. N., Jr., "Development and Application of an Interferometric System for Measuring Crack Displacements," Final Report on NSG 1148, June 1976.

12. Heywood, R. B., "Designing by Photoelasticity," Chapman and Hall Ltd., 1952, pp. 167-169, 178-181, 210-244.

13. MAR-TEST Inc., "Cyclic Stress Strain Curve for MM-247-DS at 1200F, R = 0.05," DRF 922 F-109 Program, December 1983.

14. Coker, E. G., Filon, L., "Treatise on Photoelasticity," Cambridge University Press, 1957, pp. 579-563.

15. Kawata, K., "Analyses of Yielding of Several Dovetail Joint Designs," Proceedings of the International Symposium on Photoelasticity at Illinois Institute of Technology, Pergamon Press, 1963, pp. 224-229.

16. Ruiz, C., Boddington, P. H. B., Chen, K. C., "An Investigation of Fatigue and Fretting in a Dovetail Joint," Experimental Mechanics, September 1984, pp. 208-217.

17. Peterson, R. E., "Stress Concentration Factors," John Wiley and Sons, Inc., 1974, pp. 150-196.